



Review

Design and Preparation of Biomass-Derived Carbon Materials for Supercapacitors: A Review

Yang Liu *, Jiareng Chen, Bin Cui, Pengfei Yin and Chao Zhang *

Department of Biomedical Engineering, Sun Yat-sen University, Guangzhou 510006, China; chenjr55@mail2.sysu.edu.cn (J.C.); cuib3@mail2.sysu.edu.cn (B.C.); yinpf3@mail2.sysu.edu.cn (P.Y.)

* Correspondence: liuyang56@mail.sysu.edu.cn (Y.L.); zhchao9@mail.sysu.edu.cn (C.Z.);
Tel.: +86-13822145763 (Y.L.); +86-20-39332145 (C.Z.)

Received: 27 August 2018; Accepted: 23 September 2018; Published: 25 September 2018

Abstract: The synthesis and application of biomass-derived carbon in energy storage have drawn increasing research attention due to the ease of fabrication, cost-effectiveness, and sustainability of the meso/microporous carbon produced from various biological precursors, including plants, fruits, microorganisms, and animals. Compared to the artificial nanostructured carbons, such as fullerene, carbon nanotube and graphene, the biomass-derived carbons may obtain superior capacitance, rate performance and stability in supercapacitor applications ascribing to their intrinsic nanoporous and hierarchical structures. However, challenges remain in processing techniques to obtain biomass-derived carbons with high carbon yield, high energy density, and controllable graphitic microstructures, which may require a clear understanding over the chemical and elemental compositions, and the intrinsic microstructural characteristics of the biological precursors. Herein we present comprehensive analyses over the impacts of the chemical and elemental compositions of the precursors on the carbon yield of the biomass, as well as the mechanism of chemical activation on the nanoporous structure development of the biomass-derived carbons. The structure–property relationship and functional performance of various biomass-derived carbons for supercapacitor applications are also discussed in detail and compared. Finally, useful insights are also provided for the improvements of biomass-derived carbons in supercapacitor applications.

Keywords: biomass-derived carbon; biological precursor; compositions; activation; nanoporous; structure–property relationship; supercapacitor

1. Introduction

Biomass-derived carbons, which can be referred to as one kind of humanmade carbon material, differ significantly from the naturally occurring carbons such as charcoal, graphite, and diamond. As graphite and diamond are formed from the naturally deposited carbon in the crust under either metamorphic or igneous environment with high temperature and high pressure [1,2], biomass-derived carbons are formed by converting the natural products, including plants, food microorganisms, and animal waste [3] into porous carbon materials through artificial processes such as thermal carbonization and activation [4]. During the thermal carbonization process, the biomasses are heated under high temperature and inert gas protection, while the heteroatoms in the backbones of the biomacromolecules are escaped, leaving the carbon skeletons with a porous structure. Upon subsequent activation, the remaining carbon skeletons can form interconnected 3D structures with relatively high conductivity, surface area and porosity, making them excellent candidates for energy storage applications, especially supercapacitors.

Similar to carbon nanotubes (CNT) and graphene, the biomass-derived carbons store charges via the electrical double-layer mechanism, which originated from the electrostatic interactions between the electrode and electrolyte [5]. In theory, the charge of the electrode (q) is balanced by attracting the counterions in the electrolyte to the near-surface of the electrode, while the counterions align according to the charge distribution on the electrode surface and form a layer of charges. The charges on the surface layer of the electrode and the charged layer of counter ions thus form the electrical double layer, while a potential drop spans across the region between these two layers (also called the outer Helmholtz plane), as shown in Figure 1. The behavior of this electrical double layer in solution is analogous to an electrical capacitor separated by a dielectric.

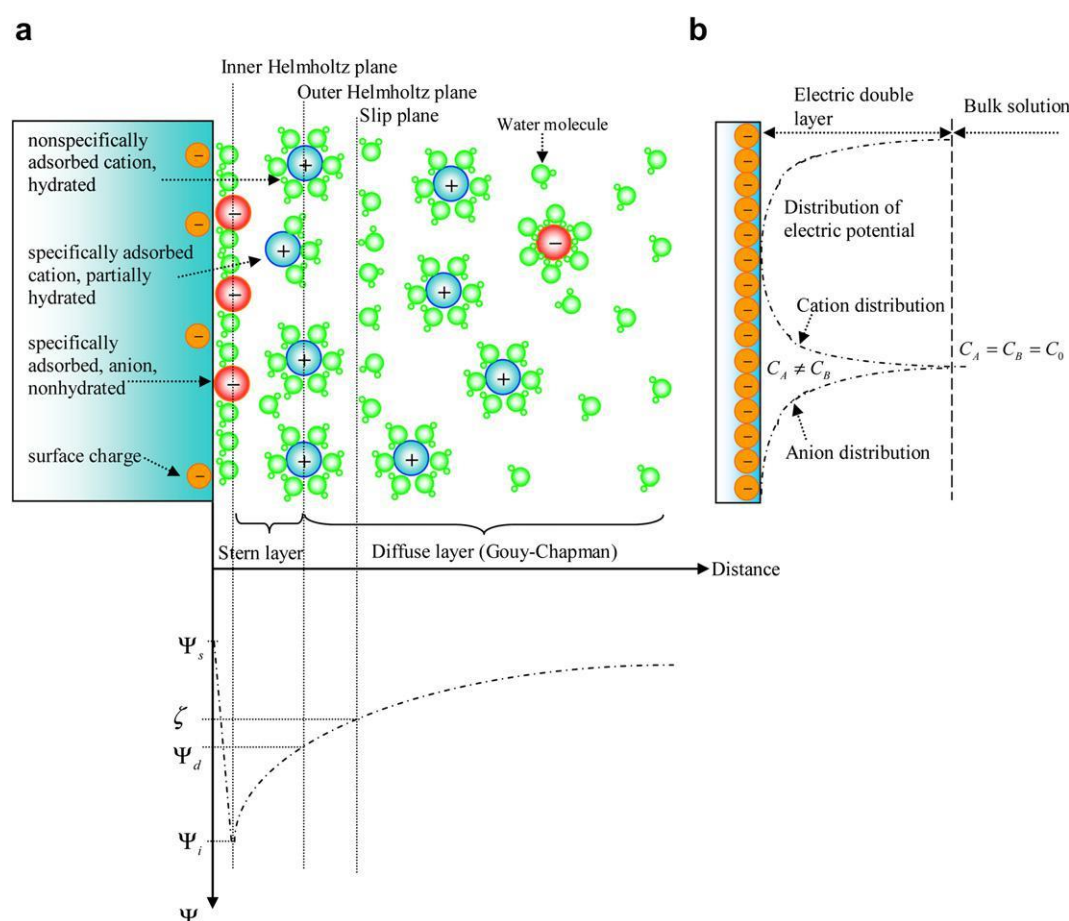


Figure 1. Schematic illustration of the (a) structure and (b) property of the electrical-double-layer in solution [6]. Reproduced from [6], with permission from Elsevier, 2010.

The supercapacitors which utilize the electrical-double-layer mechanism for charge storage can be classified as electrical double-layer capacitors (EDLC), including the biomass-derived carbons. To satisfy the functional requirements of EDLC-type supercapacitors, the biomass-derived carbons should at least attain the following properties, including: (i) large specific capacitance (C), which corresponds to high power and energy density; (ii) low equivalent series resistance (ESR), which corresponds to less voltage drop, more available power and less power loss; (iii) large surface area and appropriate pore size distribution (PSD), which corresponds to higher electrical double layer capacitance and better rate performance; (iv) cyclability and long lifetime, which corresponds to high electrode stability under repeatedly charge–discharge cycles and changed temperatures.

Extensive research efforts have been devoted to the preparation of biomass-derived carbons with heteroatom doping, high surface area, and high microporosity for their excellent performance in multiple applications, including water pollutant absorption [7,8], ionic liquid concentration [9], carbon dioxide capture [10–12], lithium-sulfur batteries [13], and supercapacitors [14–17]. Among the mentioned applications, the supercapacitor is considered one of the most suitable utilizations

for the biomass-derived carbons, since their major features are in good accordance with the above-mentioned EDLC properties. Highly specific capacitance exceeding 400 F g^{-1} can be obtained from the porous carbon flakes and nanosheets derived from human hair [18], dry elm samara [19] and orange peels [20], which is higher than many other EDLC-type supercapacitors, even carbon nanodots [21], carbon nanofibers [22] and carbon nanotubes [23] (CNT); while highly conductive biomass-derived carbons (with conductivity $\sim 1.12 \times 10^3 \text{ S m}^{-1}$) with low ESR can be obtained from the porous carbon nanosheets and nanofibrous carbon microspheres derived from chicken egg-shell membrane [24], gelatin [25], auricularia [26], and chitin [27]. Moreover, superior rate performance with over 68% capacitance retention at high current densities ($\sim 30\text{--}50 \text{ A g}^{-1}$) has been achieved for the *N,O-co*-doped, *N,S-co*-doped and *B,N-co*-doped porous carbon nanosheets derived from poplar catkins [28], willow catkins [29], and gelatin [25]. And cycle lives exceeding 15,000 cycles with capacitance retention of 79.2% and 113% have been achieved for the activated carbons derived from chicken egg white [30] and gelatin [25], respectively; while a cycle life exceeding 50,000 cycles with 98% capacitance retention has been achieved for the carbon nanosheets derived from dry elm samara [19].

In order to prepare biomass-derived carbons for supercapacitors with controlled PSD, heteroatom doping and high yield in a simple and cost-effective manner, tremendous effort has been devoted to improving the whole fabrication processes from precursor selection, carbonization and activation to electrochemical characterization. Firstly, different types of precursors were selected based on their cost, intrinsic microstructures and elemental compositions. For example, rice straw [31], wheat straw [32], pistachio [33], and poplar catkins [34] were selected as the precursors for biomass-derived carbons due to their low cost and natural abundance; while the chicken egg shell membranes [24], Auricularia [26], kombucha [35] and orange peel [20] were selected because of their unique hierarchical and porous microstructures; and the *Bacillus subtilis* [36], human hair [18] and chitin [27] were selected as a result of their relatively abundant elemental compositions of heteroatoms such as nitrogen, oxygen and sulfur. To further improve the functional properties of the precursors, i.e., electrical, nanostructural and electrochemical properties, many other functional materials, such as graphene oxide [37], boric acid [25], and melamine [32], were mixed with the biomass precursors before the carbonization/activation processes to either serve as the conducting microstructural components, hard templates for 2D long-range order or as the heteroatom source. Secondly, the pathway of carbonization and activation will be strongly dependent on the physical and chemical state of the precursor. For example, “black liquor” was synthesized from rice straw by using potassium hydroxide (KOH) aqueous solution to extract the lignin content within the straw via a hydrothermal process [31]. The black liquor was subsequently dried to obtain black solids and used for the one-step carbonization (400°C) and activation (800°C) under nitrogen atmosphere. When *Bacillus subtilis* was used as the biomass precursor, it was mixed with different activation reagents (e.g., ZnCl_2 and KOH) and directly carbonized at 800°C for 2 h in nitrogen atmosphere for tuning the elemental contents of nitrogen and oxygen, respectively [36]. And when human hair was used as the precursor, a fine cutting process to obtain small fibers ($\sim 5 \text{ mm}$ long) and their subsequent precarbonization at 300°C were required before the activation process [18]. Thirdly, besides characterizing the electrochemical performance of the biomass-derived carbons in aqueous electrolytes, i.e., 6 M KOH solution, organic (e.g., LiPF_6 in ethylene carbonate/diethyl carbonate) and ionic liquid (e.g., 1-ethyl-3-methylimidazolium tetrafluoroborate) electrolytes were also widely employed to evaluate the electrochemical capacitive performance of the biomass-derived carbons [18,38,39].

Compared to the other advanced electrode materials for EDLC-type supercapacitors, such as CNT and graphene, the biomass-derived carbons may obtain several critical advantages, including:

- (a) Cost-effectiveness: the precursors of biomass-derived carbons are cheap and abundant, which are mostly from plant organs, food and animal wastes, and microorganisms.
- (b) In-situ nanoporous structure formation: the skeleton of the biomacromolecules is preserved as they are converted to carbon under inert gas protection, forming interconnected conductive carbon structures with nanopores generated in-situ.

- (c) Versatility in products and processing: various kinds of bioprecursors can be converted into biomass-derived carbons through similar processing steps, including carbonization, activation, and purification. On the other hand, different chemicals, i.e., metallic compounds, can be introduced to the conversion process which further endow the biomass-derived carbons with exceptional electrochemical capacitive and catalytic properties.
- (d) Environmentally friendly: compared with the synthesis processes of CNT and graphene, the fabrication of biomass-derived carbons does not require high-pressure conditions and harsh chemicals, therefore it is more energy-saving and environmentally friendly. On the other hand, the utilization of biowastes as precursors to fabricate high-performance biomass-derived carbons also represents the state-of-the-art green pathway to obtain functional carbon materials.

As the starting point to prepare the biomass-derived carbons, the selection of biomass precursors is critical to the final production of inherited biomass-derived carbons of a high carbon yield, high content of heteroatom doping, and interconnected 3D nanoporous structure, which are essential for the supercapacitor application. The chemical composition, elemental composition, and microstructural characteristic of the biomass precursor would have significant impacts on the carbon yield, doping level and microporosity of the derived carbon material. Providing with the diverse types of precursors that have been used for the preparation of biomass-derived carbon, it is urgent to formulate a general strategy for selecting the precursors with appropriate chemical, elemental compositions and nanoporous characteristics to achieve heteroatom-doped activated carbons with hierarchically interconnected meso/microporous structures designated for high-performance supercapacitor applications.

2. Precursors

Various biomaterials have been utilized to fabricate biomass-derived carbons, including poplar catkin, lignin, dry elm samara, bacterial cellulose, egg white, rice, orange peel, mushrooms, chitin, and human hair, etc. [14,18–20,28,30,40–43]. However, these biomaterials can all be categorized into four major types, i.e., the plant-based, food-based, microorganism-based, and animal-based biomass. By understanding the chemical and elemental compositions of different types of biomass, one can precisely predict the composition and structure of the corresponding biomass-derived carbons.

Even though the major research attention in biomass-derived carbons has been drawn to the search of unique biomass precursors which simultaneously possess high carbon contents, hierarchical nanoporous structures and heteroatom compositions that are extremely beneficial for the formation of interconnected meso/microporous structure and N/O-containing surface functional groups during the carbonization/activation processes, by which would greatly enhance the corresponding EDLC-supercapacitor application. But low yields are often associated with the advanced precursors. For example, the biochar derived from chicken egg shell membrane did show excellent supercapacitive properties including high specific capacitance, high conductivity and long cycle life [24]. But the yield of egg shell membrane from the egg is extremely low (~0.2–0.25 g/per egg) [44], regardless of the weight loss during carbonization and activation, which make the whole fabrication process more tedious and less economic sound. The situation is the same for the biochar derived from willow catkins, which also shows excellent supercapacitive properties of high capacitance, long cycle life and high rate performance [29]. But the final carbon yield after activation is only 5.5 wt %, which is substantially lower than other biomass precursors such as lignin [40] (40.3 wt %), okara [45] (52.1 wt %) and rice straw [31] (24.8%). Moreover, the biochar yields of the precursors differ from their biological types, such as wheat stalk [46] (11.3 wt %), popcorn [41] (18.7 wt %) and *Auricularia* [26] (17 wt %). Since the biochar yield, microstructure and heteroatom doping level of the biomass-derived carbon are heavily dependent on the chemical structure and elemental composition of the precursors as well as their conformation and intermolecular configurations, therefore it is critical to investigate and understand the characteristics of the precursors at the molecular and elemental level, where significant insights over the molecular and elemental engineering of the precursors can be given for the generation of

biochar with optimized supercapacitive properties, which will be described detailly in the below sections.

2.1. Plant-Based Biomass

In general, the quantitative chemical compositions of the plant-based biomass differ from one species to another; even for different organs of the same plant, the chemical compositions change quantitatively. On the other hand, even originated from different species, the qualitative chemical compositions of plant-based biomass share mutual components, including lignin, cellulose, hemicellulose and extractives. The representative qualitative and quantitative chemical compositions of common plant-based biomass are shown in Table 1.

Table 1. Chemical compositions of different plant-based biomass (in dry weight % basis).

Biomass	Moisture (%)	Lignin (%)	Cellulose (%)	Hemicellulose (%)	Extractives (%)	References
Coconut coir	13.68	46.48	21.46	12.36	8.77	[47]
Coconut sheath	5.90	29.7	31.05	19.22	1.74	[47]
Bagasse	5.64	22.56	39.45	26.97	4.33	[47]
Banana leaf	11.69	24.84	25.65	17.04	9.84	[47]
Sisal	-	7.6–9.2	43–56	21–24	-	[47]
Corn stover	-	18–22	37–42	20–28	-	[48]
Wheat straw	-	16–24	31–44	22–24	-	[49]
Rice straw	-	10–18	32–41	15–24	-	[49]
Barley straw	-	8–17	33–40	20–35	-	[49]
Switchgrass	-	12–23	33–46	22–32	-	[49]
Palm shell	-	53.4	29.7	-	-	[50]
Olive waste	-	28.0	44.8	-	-	[51]
Jute	-	11.8	64.4	-	-	[52]
Abaca	-	5.1	63.2	-	-	[52]
Flax	-	2.5	56.5	-	-	[52]
Hemp	-	3.3	67.0	-	-	[52]
Scots pine stem wood	-	27.0	40.7	26.9	5.0	[53]
Scots pine bark	-	13.1	22.2	8.1	25.2	[53]
Scots pine branches	-	21.5	32.0	32.0	16.6	[53]
Scots pine needles	-	6.9	29.1	24.9	39.6	[53]
Scots pine stump	-	19.5	36.4	28.2	18.7	[54]
Scots pine roots	-	29.8	28.6	18.9	13.3	[54]
Poplar leaves	-	23.2	22.3	12.8	40.0	[55]
Alder leaves	-	12.4	15.0	13.3	44.7	[55]
Willow leaves	-	20.0	18.5	14.7	43.4	[55]
Apricot pit shell	-	31.91	34.31	-	-	[56]
Sunflower seed hull	11.8	28.7	31.3	25.2	-	[57]

The relationships between the chemical compositions of different plants and different plant organs are clearly demonstrated in Table 1. It can be observed that the seed shells of Arecaceae (coconut, palm, etc.) contain high fractions of lignin and cellulose components (>65%), especially for the palm shell, the combined fraction of lignin and cellulose is around 83%. On the other hand, the bast plant fibers generally contain more fractions of cellulose, for example, the cellulose fractions of jute, flax, and hemp are 64.4%, 56.5%, and 67.0%, respectively; these values are substantially higher than the other plant parts such as wheat straw (31–44%), switchgrass (33–46%), Scots pine stem wood (40.7%), and poplar leaves (22.3). The chemical structures of lignin and cellulose are shown in Figure 2a,c. Besides lignin and cellulose, the plant organs also contain hemicellulose and extractives. The hemicellulose can be referred to a class of short-chain (500–3000 sugar units), highly branched polysaccharides consisting of five- and six-carbon sugars (Figure 2b), including xylose, arabinose, glucose, galactose, mannose and fucose [58]. The extractives can be referred to as the organic and inorganic compounds that reside in the lignocellulosic tissues, including triglycerides, steryl esters, fatty acids, phenolics, terpenoids, calcium, potassium, magnesium, etc. [59].

The elemental compositions of the precursors are also worthy of investigation, as the oxygen and nitrogen contents of the precursor can significantly influence the yield, microstructure,

conductivity, and capacitance of the corresponding biomass-derived carbon products. It has been realized that the precursors with higher oxygen contents may derive carbon with less yields, more defects and less crystallinity, as more volatile compounds are released during thermal process on the biomass surface with high oxygen content [60,61]. While precursors with higher nitrogen contents can derive intrinsically nitrogen-doped carbons with better electrochemical properties [62]. The elemental compositions of typical plant-based precursors are shown in Table 2.

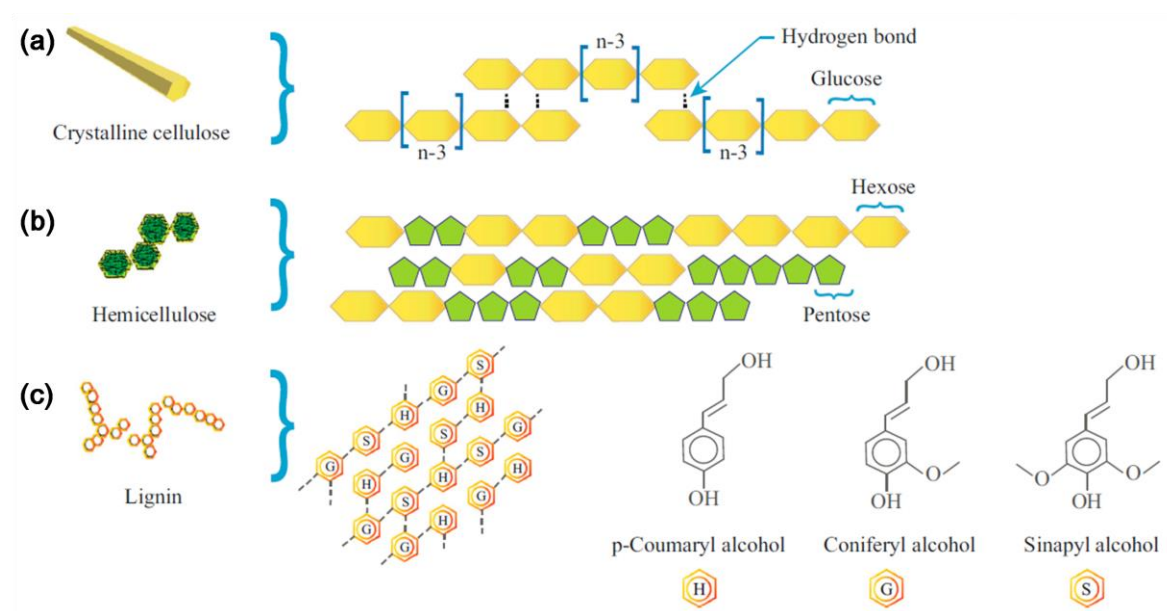


Figure 2. Chemical structures of (a) cellulose, (b) hemicellulose and (c) lignin with the monomeric units of lignin macromolecules labeled as H, G and S. Reproduced from [49], with the permission from Springer Nature, 2015.

During the thermal carbonization process, the contents of plant-based biomass will be eventually converted to the biomass-derived carbon. Even though the carbon fractions of the plant-based biomass are relatively high (40–60%) according to their elemental compositions, the actual carbon yield of the conversion is highly dependent on their chemical compositions, especially the mass fractions of lignin, cellulose and hemicellulose. Lignin, which signifies the highest thermal stability among these components, is measured to be the major contributor to all chars and activated carbons [63]. On the other hand, for cellulose and hemicellulose, which are less thermally stable than lignin, can only contribute low to moderate carbon contents to the final chars. This is especially the case for cellulose, which underwent ~78% weight loss by heating at 400 °C for 1 h [60]. The respective contributions of lignin, cellulose and hemicellulose to the carbon yields of different biomass are shown in Table 3. It was also found that the value of biochemical oxygen demand (BOD) of the biochars increased with higher cellulose content of the precursors, which indicated the trend of non-aromatic carbon formation induced by the cellulose components [64]. However, evidences were also shown that all the lignin, cellulose and hemicellulose components contributed to the porosity of the final carbons, regardless of their weight fractions [63]. It was also found that no significant interaction between cellulose and hemicellulose existed during thermal pyrolysis at 500 °C; while apparent interactions were found between the cellulose and lignin components of herbaceous biomass, resulting in a decreased yield of levoglucosan and increased low molecular weight compound and furan yields; and no apparent interaction was found between the cellulose and lignin components of woody biomass [65]. Therefore, it is rather clear that one should select plant-based biomass with (i) high lignin fraction, (ii) low cellulose fraction, (iii) low oxygen fraction and (iv) high nitrogen content in order to obtain plant-based biomass-derived carbons with high yield, higher degree of graphitization, controllable defects and good conductivity, which are desired for high-performance supercapacitive materials.

Table 2. Elemental compositions of different plant-based biomass (in dry weight % basis).

Biomass	C (%)	H (%)	O (%)	N (%)	S (%)
Coconut coir [47]	46.22	5.44	40.47	0.36	-
Coconut sheath [47]	42.23	5.69	45.57	0.44	-
Bagasse [47]	48.6	6.3	45.1	-	-
Banana leaf [47]	44.01	6.10	38.84	1.36	-
Hybrid poplar [66]	48.45	5.85	43.69	0.47	0.01
Poplar, DN 34 [67]	50.02	6.28	42.17	0.19	0.02
Hybrid poplar, DN 34 [68]	51.73	4.47	35.11	0.24	0.03
Corn stover [69]	43.65	5.56	43.31	0.61	0.11
Switchgrass [69]	47.75	5.75	42.37	0.74	0.08
Wheat straw [69]	43.20	5.00	39.40	0.61	0.11
Ponderosa pine [69]	49.25	5.99	44.36	0.06	0.03
Yellow poplar [70]	64.5	5.89	29.2	0.26	-
Kraft lignin [71]	57.83	3.42	33.66	0.47	4.62
Rubber seed shell [72]	48.8	5.9	43.7	1.5	0.1
Rubber seed kernel [72]	64.5	8.2	23.4	3.6	0.3
Saline corn stem [73]	44.51	5.90	43.90	0.84	0.16
Saline corn leaves [73]	41.27	5.86	43.86	1.30	0.24

Table 3. The weight contributions of lignin, cellulose and hemicellulose to the carbon yields of different biomass [63].

Biomass	Lignin (Lc %)	Cellulose (Cc %)	Hemicellulose (Hc %)	Calculated Yield (%)	Experimental Yield (%)	Standard Deviation (%)
Coconut shell	66.9	8.7	24.4	30.8	25.6	2.6
Apple pulp	58.0	18.8	23.1	16.2	25.7	4.8
Plum pulp	79.0	5.6	15.4	22.2	25.9	1.9
Plum stones	70.8	14.1	15.1	31.1	24.6	3.3
Olive stones	75.3	10.7	14.1	25.1	30.9	2.9
Sulphuric acid treated olive stones	64.8	19.0	16.2	29.1	27.4	0.9
Soft wood	55.0	27.6	17.4	24.9	21.3	1.8
Synthetic coconut shell	66.9	8.5	24.5	33.5	32.7	0.4

2.2. Fruit-Based Biomass

Similar to the plant-based biomass, the fruit-based biomass may differ in the quantitative chemical compositions with respect to the species, condition of growth, and different fruit parts. However, the qualitative chemical compositions of fruit-based biomass are also sharing several major components, including crude fibers, crude proteins, lipids, ash and carbohydrates [74,75]. The chemical compositions of typical fruit-based biomass are shown in Table S1.

As shown in Table S1, the fruit-based biomass contains more moisture, crude protein and lipids as compared to the plant-based biomass. The typical crude protein contents in the pulp and peels of the fruit-based biomass in Table S1 are from 4.4% to 14.8% and from 2.8% to 18.06%, respectively; While the typical lipid contents in the pulp and peels are from 1.4% to 28.6% and from 0.7% to 9.96%, respectively. Thus, the overall crude protein plus lipid contents in the fruit pulp and peels are in the range from 5.8% to 43.4% and from 3.5% to 28.02%, respectively. However, the high fractions of crude proteins and lipids provide limited contribution to the yield of carbon during the thermal carbonization process, since both of them degrade at relatively low temperature (<300 °C), releasing volatile compounds such as carbon dioxide (CO₂), water vapor (H₂O), ammonia gases (NH₃), olefins and methyl esters [76,77]. On the other hand, the high nitrogen and phosphorus contents of crude protein and lipids may assist the in-situ formation of heteroatom-doped carbons. Like the plant-based biomass, the crude fibers which are composed of lignin, cellulose and hemicellulose may provide major contribution to the carbon yields for the fruit-based biomass. However, the mass

fractions of crude fibers are in the range from 12.16% (pawpaw) to 43.9% (avocado) in the peels of the fruit-based biomass, and from 1.8% (Papaya) to 41.1% (Avocado) in the pulp, as shown in Table S1. These values are substantially lower than the values of plant-based biomass according to Table 1. Furthermore, the crude fibers of the fruit-based biomass are generally rich in cellulosic components rather than lignin [78], which make them rather insufficient in generating biomass-derived carbons with high yield and graphitic structures.

2.3. Microorganism Based Biomass

Besides plants and their fruits, biomass-derived carbons can also be produced from microorganisms, such as Fungi and bacterial cellulose. Fungi, including mushrooms (Figure 3a,c) and yeasts (Figure 3b,d), are considered good regenerative biomass precursors for generating biomass-derived carbons, ascribing to their abundance in nature and fast growth rate.

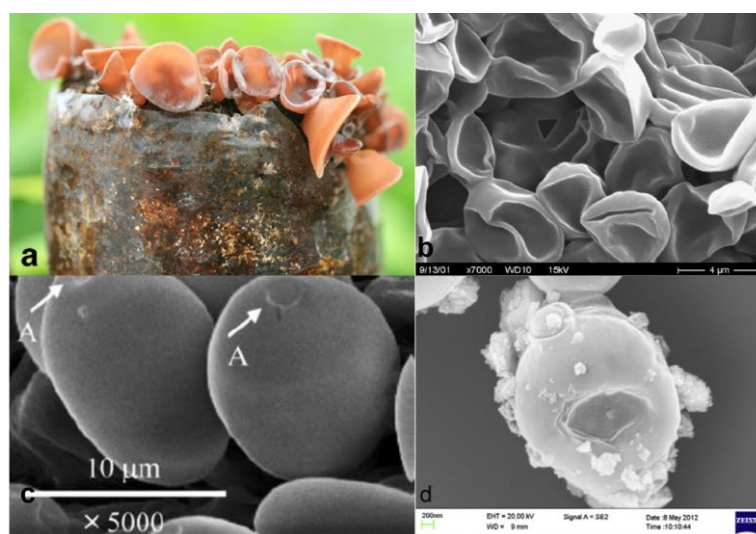


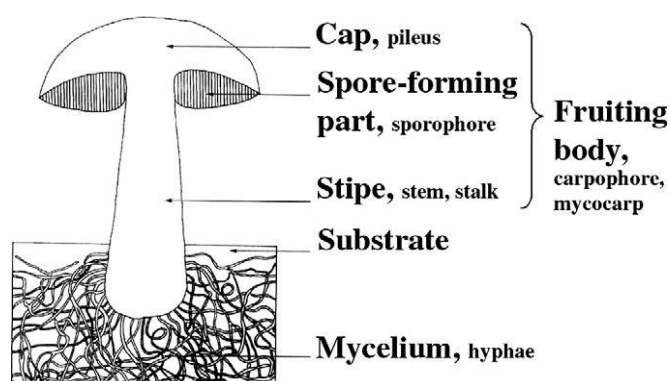
Figure 3. Photographs of (a,b) the bulk and (c,d) cellular structures of (a,c) mushrooms and (b,d) yeasts, respectively [the species shown in the images are (a) *Auricularia thailandica*, (b,d) *Saccharomyces cerevisiae* and (c) *Psilocybe cubensis*. The arrow in C indicated the germ spores. (a) Reproduced from [79], with permission from Springer Nature; 2017. And (b) from [80], (c) from [81], (d) from [82], with permission from Elsevier 2003, 2003 and 2015.

The chemical compositions of typical microorganisms are shown in Table 4, refs. [83–92] which lists the major components of microorganism-based biomass, including carbohydrates, crude proteins, crude fibers, crude fat, and ash. Even though the nomenclatures of the major components of the microorganism-based biomass are similar to the plant- and fruit-based biomasses, the actual molecules and elements comprising these components are substantially different. For example, the carbohydrates of the microorganism-based biomass are consisting of chitins, which are bio-crosslinked with glucan and can serve as a primary source of carbon during thermal carbonization [93]; while the main carbohydrates in the plant/fruit-based biomasses are sucrose and starch, which are non-crosslinked with low thermal stability [94]. On the other hand, the crude fibers of the microorganism-based biomass are majorly composed of cellulose, which shows similar carbonization behaviors to the plant/fruit-based biomasses, and can also provide important contribution to the yield of carbon. Other components, such as crude protein, crude fat and ash, may decompose rapidly during the thermal carbonization process, generating volatile and low molecular weight compounds which provide neglectable contribution to the carbon yield.

Table 4. Chemical compositions of typical microorganisms, including mushrooms and fungi (the values are presented in dry weight % basis).

Microorganisms	Carbohydrates	Crude Fiber	Crude Protein	Crude Fat	Ash	References
Agaricus bisporus	42.56	13.21	33.85	2.41	7.97	[83]
Auricularia thailandica	17.36	4.62	12.99	2.93	4.30	[79]
Aspergillus nidulans	60.5	-	10.0–10.4	9.5	-	[84]
B. aureus	34.0	17.0	26.9	2.1	8.5	[85]
B. edulis	30.6	15.3	28.7	4.1	9.2	[86]
B. speciosus	28.6	21.0	28.1	2.9	7.6	[86]
C. aureus	61.5	5.2	14.1	4.0	9.2	[87]
Lactarius deliciosus	25.0	36.3	20.2	2.5	7.5	[88]
Lactarius hatsudake	38.2	31.8	15.3	1.0	7.3	[88]
Lactarius volemus	15.0	40.0	17.6	6.7	13.3	[88]
L. crocipodium	12.8	37.9	29.3	1.0	5.8	[86]
Lentinula edodes	30.2	39.4	17.1	1.9	4.3	[89]
Pleurotus ostreatus	57.05	8.25	26.05	2.79	5.86	[83]
R. virescens	13.4	32.8	28.3	1.5	11.9	[88]
S. aspratus	64.6	5.1	12.0	2.8	10.4	[90]
T. matsutake	36.7	29.1	14.3	5.0	8.9	[91]
Tricholoma portentosum	34.6	30.1	19.6	5.8	9.9	[92]
Tricholoma terreum	31.1	30.1	20.1	6.6	12.1	[92]

Mushrooms are the major precursors to produce biomass-derived carbons in the category of microorganism-based biomass. To speak more specifically, the fruiting body of mushrooms are frequently used for the fabrication of biomass-derived carbon, rather than the other parts such as mycelium. A schematic illustration of the functional components of the mushrooms is shown in Figure 4 [95]. Compared to the plant- and fruit-based biomass, the mushrooms are attractive as the carbon precursors due to their high nitrogen content. The nitrogen contents of mushroom are within the range between 3–10% (in dry weight % basis), some species can even reach 17% [96–98]. Therefore they are promising precursors to produce intrinsically nitrogen-doped biomass-derived carbons. However, the elemental compositions of mushroom are heavily dependent on their growth substrates and growing conditions [96,97], which means the elemental compositions of the mushrooms may change from one specific growth region to another.

**Figure 4.** Schematic illustration of the individual functional components of the mushrooms. Reproduced from [95], with permission from Elsevier, 2009.

2.4. Animal-Based Precursors

Due to its natural abundance, high nitrogen content and chemical stability, chitin is another promising bio-based precursor for the production of biomass-derived carbon. Different from cellulose, chitin is capable of forming (i) intensive intermolecular hydrogen bonds, (ii) crosslinking networks of chitin-glucan and chitin-catecholamine complexes [99,100], which endow chitin with substantially higher thermal stability than cellulose and higher carbon yields. Many types of animal, including crustaceans, insects and mollusks can be used as the primary sources for chitin extraction, which further provide economic, green and recyclable ways for the production of biomass-derived

carbon [101]. The representative types of animal for chitin sourcing and their corresponding chitin contents are shown in Table 5.

Table 5. Typical types of animal for chitin sourcing and their chitin contents.

Crustaceans	Chitin (%)	References	Insects	Chitin (%)	References	Mollusks	Chitin (%)	References
Cancer (crab)	72.1	[101]	Periplaneta (cockroach)	2.0	[101]	Clam	6.1	[101]
Carcinus (crab)	64.2	[101]	Blatella (cockroach)	18.4	[101]	Shell oysters	3.6	[101]
Paralithodes (king crab)	35.0	[101]	Coleoptera (ladybird)	27–35	[101]	Squid pen	41.0	[101]
Callinectes (blue crab)	14.0	[101]	Diptera pupae	54.8	[101]	Krill, deproteinized shells	40.2	[101]
Crangon and Pandalus (shrimp)	17–40	[101]	Pieris pupae (butterfly)	64.0	[101]	-	-	-
Alaska shrimp	28.0	[101]	Bombyx (silk worm)	44.2	[101]	-	-	-
Pandalus borealis (shrimp)	17–20	[102]	Galleria (wax worm)	33.7	[101]	-	-	-
Nephro (lobster)	69.8	[101]	Holotrichia parallela (beetle)	15	[103]	-	-	-
Homarus (lobster)	60–75	[101]	Brachytrupes portentosus (house cricket)	4.3–7.1	[104]	-	-	-
Lepas (goose barnacle)	58.3	[101]	Cicada sloughs	36.6	[105]	-	-	-
Portunus pelagicus (crab)	20.24	[106]	Ceas variabilis (grasshopper)	9.93	[107]	-	-	-

According to Table 5, the cuticles of many crustaceans, i.e., Cancer, Carcinus, Crangon, Pandalus, contain relatively high contents of chitin ranged from 17% to 72%; and the cuticles and sloughs of several insects, including Blatella, Coleoptera, Holotrichia parallela, the pupae of Diptera and butterflies, and the sloughs/pupa exuvia of cicada and silk worm, also contain remarkable chitin contents ranged from 18.4% to 64.0%. However, before the chitin contained in these biomasses can be used, mechanical and chemical processes are required to extract chitin from the biomasses, which may involve the mechanical grinding, chemical demineralization and deproteinization [108]. During the extraction process, impurities such as ashes, proteins and dyes are removed from the biomass, leaving the purified chitin components. The yields of the extraction process are varied according to different biomass precursors and mechanical/chemical processing methods, which settle within the range from 4% to 40% in the reported literatures [107,109]. Similar to the microorganism-based biomass, chitin extracted from the animal-based biomass also shows relatively high nitrogen contents (~6%) [110], which further indicates its promising applications in the in-situ generation of the nitrogen-doped biomass-derived carbon. The elemental compositions of chitin obtained from different animal-based biomasses are shown in Table 6.

Besides the cuticles and sloughs of animals, the hairs, horns, claws and hooves of animals are also good precursors for producing the biomass-derived carbons. Different from the cuticles and sloughs, the hairs, horns, claws and hooves of the animals are majorly consisting of fibrous structural proteins, called “keratin” [111,112]. There exists two types of keratin, α -keratin and β -keratin, by which the primary structures are consisting of amino acids, as shown in Table S2. Similar to chitin, keratin also attains significant chemical and thermal stability as a result of its intensive intermolecular bonding. Three types of intermolecular bonding are existed within the

supercoil motifs of keratin, including (i) non-covalent hydrogen bonds, (ii) ionic salt bonds, and (iii) covalent disulfide cystine crosslinking, as shown in Figure 5. Due to the strong covalent and non-covalent bonding within its molecular structure, keratin shows sufficient stability during the thermal carbonization process, generating high-quality biomass-derived carbons in high yield. One notable example is the human hair-derived heteroatom-doped carbon flakes, which showed high specific surface area, high capacitance and long-term cycling stability as the electrode material for supercapacitors [18].

Table 6. Elemental compositions of chitin obtained from different animal-based biomasses (in dry weight % basis).

Biomass	Chitin C (%)	Chitin H (%)	Chitin N (%)	C/N	References
<i>Pariplaneta americana linnaeus</i>	47.3	7.32	7.20	6.57	[109]
<i>Apis mellifera linnaeus</i>	52.65	8.42	5.55	9.49	[109]
<i>Holotrichia parallela</i>	44.36	5.92	6.45	6.88	[106]
<i>Brachytrupes portentosus</i>	41.30	-	6.022	6.858	[104]
Commercial shrimp	43.61	-	4.794	9.10	[104]
<i>Portunus pelagicus</i>	77.67	12.71	9.62	8.07	[103]

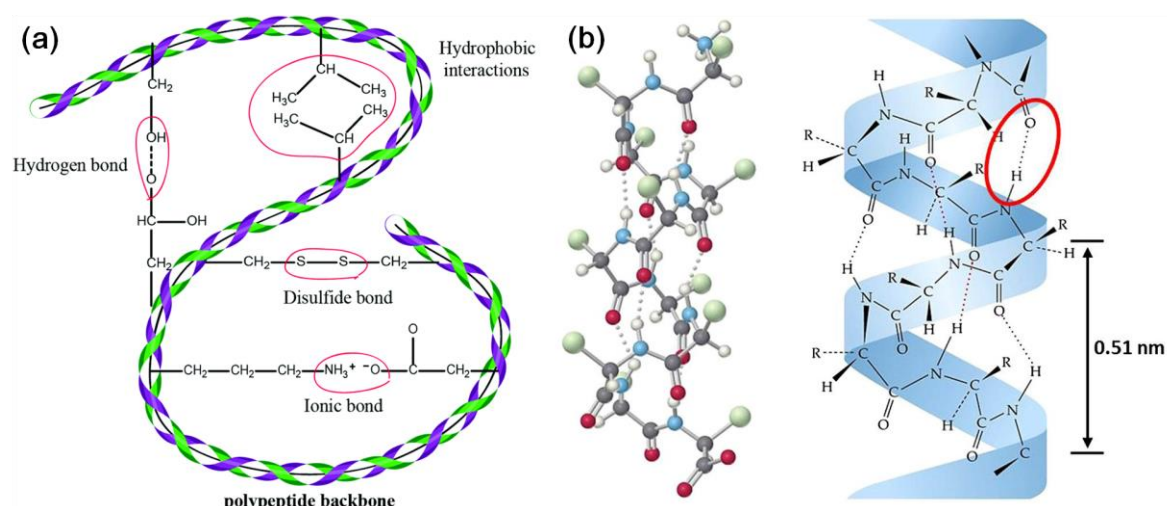


Figure 5. Schematic illustrations of the (a) intermolecular bonding and (b) intermediate filament structure of α -keratin. Reproduced (a) from [113], with permission from Royal Society of Chemistry, 2017. And (b) from [114], with permission from Elsevier, 2016.

2.5. Principles for the Precursor Selection of Biomass-Derived Carbon

In the previous sections, the chemical and elemental compositions of the plant-, fruit-, microorganism- and animal-based biomasses have been comprehensively analyzed. The relationships between the chemical and elemental compositions of the biomass and their contribution to the as-obtained biochars have also been discussed in detail. To fabricate biomass-derived carbons with high quality (high conductivity, high porosity, etc.) and high yield for supercapacitor applications, the following criteria should be considered:

- The precursor biomass should contain high contents of highly crosslinked, high molecular weight, and thermally stable biomacromolecules, such as lignin, chitin and keratin, for higher rate of aromatic carbon formation and higher yield of carbon during the thermal carbonization process.
- The precursor biomass should contain low contents of non-crosslinked, low molecular weight, and aliphatic compounds, which provide insignificant contribution to the yield of carbon and impede the formation of aromatic carbon by generating volatile compounds that prevent fusion and flow.

- (iii) The precursor biomass should contain low elemental contents of oxygen for the oxygen would impede the aromatic carbon formation and increase the biochemical oxygen demand (BOD); while it should contain high elemental contents of nitrogen for the in-situ generation of nitrogen-doped carbon with higher conductivity.

3. Structures and Properties

The biomass-derived carbons prepared by using the thermal carbonization and chemical activation may exhibit the morphology of porous nanosheets, as shown in Figure 6. This phenomenon can be attributed to the permeation of the activation reagents, i.e., potassium hydroxide (KOH) and zinc chloride (ZnCl_2), into the carbonized biomass skeletons and their intensive interactions with the carbon basal planes [115]. For example, the using of KOH as the activation reagent may involve the following mechanisms, including: (i) Chemical activation, etching of the carbon skeletons by the redox reactions between carbon (C) and KOH, which generates intensive microporosity within the carbon structure; (ii) Physical activation, emerging of the gasified products, i.e., water (H_2O) and carbon dioxide (CO_2) vapors, from the redox reactions between carbon and potassium ions, which further promotes the porous structure formation; (iii) the intercalation of metallic K into the graphitic structures of the carbon skeleton, which expands the lattice spacing of the graphitic carbon and subsequently generates the exfoliated nanosheet-like carbon nanostructures [116]. After the activation process, the specific surface area (SSA) of the biomass-derived carbons increases drastically, as a result of the development of microporosity and the formation of nanosheets, and tens- or hundreds-fold increments in SSA can be achieved after KOH activation [20,36,117]. A schematic illustration of the effects of KOH activation on the porosity of carbon structure is shown in Figure 7.

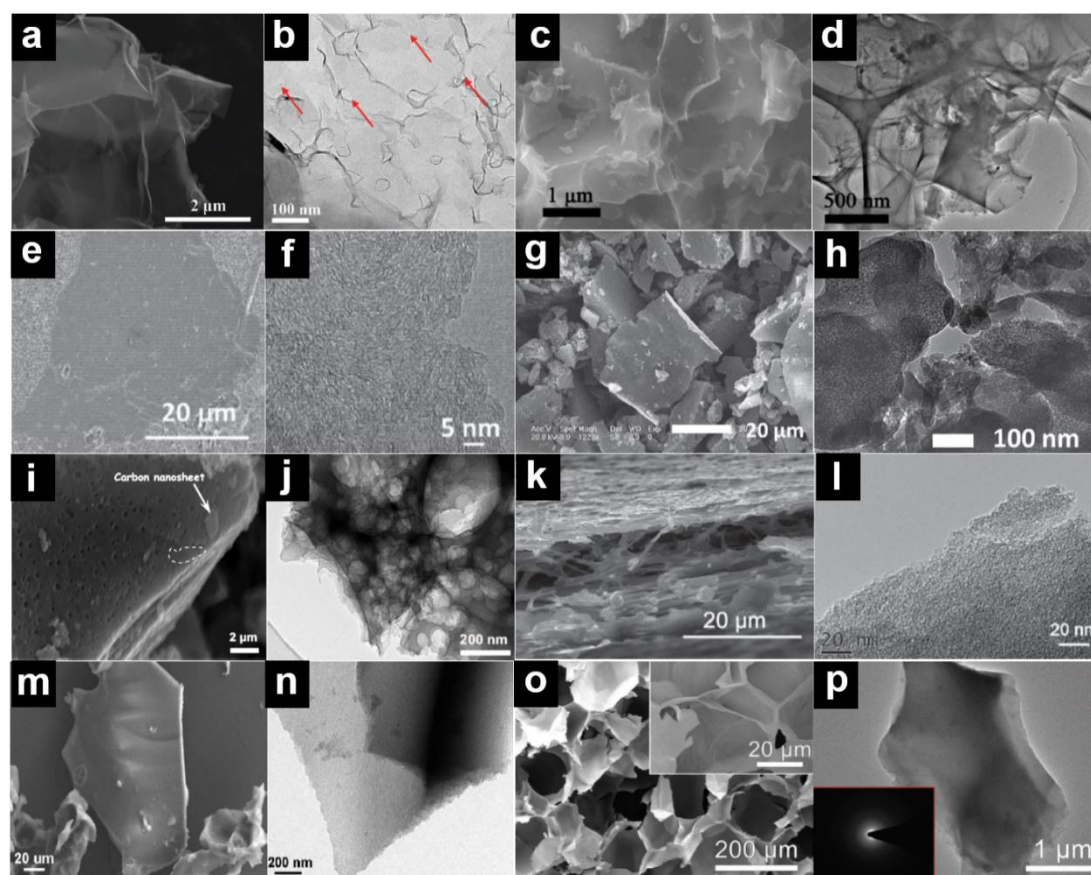


Figure 6. SEM and TEM images biomass-derived carbons produced from various precursors, including (a,b) highly graphitic carbon nanosheets from wheat stalk. Reproduced from [46], with permission from Royal Society of Chemistry, 2016; (c,d) N,S-doped porous carbon nanosheets from

willow catkin. Reproduced from [29], with permission from Elsevier, 2016; (e,f) B/N co-doped carbon nanosheets from gelatin. Reproduced from [25], with permission from John Wiley and Sons, 2015; (g,h) heteroatom-doped carbon from microorganism (*Bacillus subtilis*). Reproduced from [36], with permission from John Wiley and Sons, 2012; (i,j) porous graphene-like carbon from fungus (*Auricularia*). Reproduced from [26], with permission from Elsevier, 2015; (k,l) carbonized eggshell membrane from chicken eggshell. Reproduced from [24], with permission from John Wiley and Sons, 2012; (m,n) hair-derived micro/mesoporous carbon from human hair. Reproduced from [18], with permission from Royal Society of Chemistry, 2014; (o,p) puffed rice derived carbon from rice. Reproduced from [41], with permission from John Wiley and Sons, 2017. Insets show the corresponding magnified SEM image and SAED pattern, respectively.

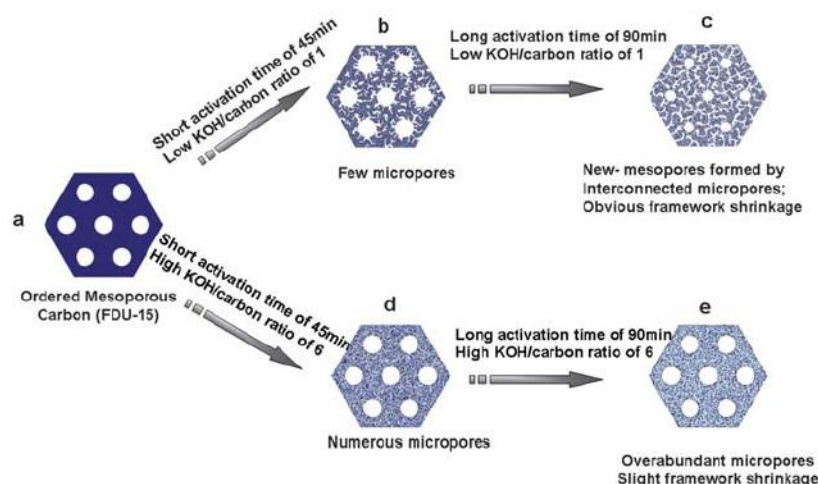


Figure 7. (a–e) Schematic illustration of the effects of KOH activation on the porosity development. Reproduced from [115], with permission from Royal Society of Chemistry, 2012.

The major parameters that determine the effect of chemical activation are the mass ratio between the activation reagent and carbon feedstock, as well as the temperature (T) and time (t) of the activation process. During the activation process, the carbon feedstock is mixed with the activation reagent at the mass ratio between 1:1 and 1:6. And then the mixture is thermally treated at a relatively high temperature (between 300 and 900 °C) for a duration between 0.5 and 2 h, where a slow heating rate and inert gas protection are simultaneously applied. It has been observed that at low KOH/C mass ratios (~ 1), the activation would induce the shrinkage of the mesopores (~ 5 nm) of the carbon feedstock [115]. Precisely, the newly generated micropores (~ 1.5 nm) by KOH etching will grow and coalesce to form the interconnected mesoporous structures, resulting in the shrinkage of the carbon framework. On the other hand, at high KOH/C mass ratios (~ 6), the activation will generate intensive micropores in the carbon framework, as the interlattice spacing is saturated with metallic K, expansions in the carbon framework are expected and observed. Because of the framework expansion, the coalescence of the micropores is significantly impeded at high KOH/C ratios, resulting in isolated micropores rather than interconnected meso/microporous structure. These speculations are further evidenced by the structural data of the activated carbon shown in Table 7. According to Table 7, the unit cell size of the activated carbon obtained from low KOH/C ratios (KF1-90) showed 3.9% shrinkage as compared to the carbon feedstock (FDU-15), which indicated the shrinkage of carbon framework. Moreover, the SSA and pore volume (PV) of KF1-90 are $1410 \text{ cm}^2 \text{ g}^{-1}$ and $0.73 \text{ cm}^3 \text{ g}^{-1}$, which are the highest among all the activated samples and evidence the formation of interconnecting meso/microporous structures within the carbon framework. On the contrary, the activated carbon obtained from high KOH/C ratios (KF6-90) showed 3.9% expansions in the unit cell size compared with FDU-15, and it also showed a high microporosity ($\sim 80\%$) and high micropore volume ($\sim 0.40 \text{ cm}^3 \text{ g}^{-1}$). But relatively low SSA ($\sim 1200 \text{ m}^2$

g^{-1}) and PV ($\sim 0.56 \text{ cm}^3 \text{ g}^{-1}$) were associated with KF6-90, indicating the formation of isolated microporous structure which is not accessible by nitrogen during the BET surface area test [115].

Table 7. Structural data (e.g., unit cell size, surface area and pore volume) of the activated carbon prepared from low to high KOH/C ratio. FDU-15 represents the pristine ordered mesoporous carbon, while $\text{KF}x\text{-}y$ represents the KOH activated FDU-15, x represents the KOH/C ratio and y represents the activation time. Reproduced from [115], with permission from Royal Society of Chemistry, 2012.

Activated Carbon	Unit Cell Size (nm)	BET Surface Area ($\text{cm}^2 \text{ g}^{-1}$)	Pore Volume ($\text{cm}^3 \text{ g}^{-1}$)	Micropore Surface Area ($\text{cm}^2 \text{ g}^{-1}$)	Microporosity (%)	Micropore Volume ($\text{cm}^3 \text{ g}^{-1}$)
FDU-15	10.2	660	0.44	180	27	0.07
KF1-45	10.7	930	0.49	590	63	0.24
KF1-60	10.2	1030	0.52	660	64	0.27
KF1-90	9.8	1410	0.73	890	63	0.38
KF4-45	10.5	1150	0.56	830	72	0.34
KF4-60	10.3	1310	0.62	1030	79	0.43
KF4-90	10.3	1240	0.59	970	78	0.40
KF6-45	10.7	1280	0.59	990	77	0.41
KF6-60	10.6	1400	0.69	1020	73	0.42
KF6-90	10.6	1200	0.56	960	80	0.40

The biomass-derived carbons obtained from low KOH/C ratios ($\sim 1\text{--}3$) did show excellent supercapacitive properties including high SSA, high rate performance and high specific capacitance, such as the biochar derived from *Auricularia*, dry elm samara, kombucha and popcorn [12,19,26,35]. It has been shown that even a higher SSA can be obtained at high KOH/C ratio, the actual supercapacitor performance was compromised because of the increased pore volume significantly lowered the volumetric capacitance of the electrode material, as shown in Figure 8 [26]. The activation temperature is also critical for the fabrication of biomass-derived carbon with appropriate supercapacitive properties. For example, egg white was carbonized and activated at different temperatures of 700, 800, 900, 1000 °C, as the activated carbon obtained at 900 °C showed the highest SSA and pore volume with appropriate pore size distribution, as shown in Figure 9 [30]. An interconnected meso/microporous structure can also be observed from the pore size distribution of the egg white activated at 900 °C, as shown in Figure 9b. The peak with the highest intensity for the micropores ($\sim 0.8\text{--}1.4 \text{ nm}$) can be observed for the eAC-900, and the evolution of the mesopores between 2–10 nm was also clearly observed, indicating the formation of interconnected meso/microporous structure. The temperature-dependent pore structural formation was also observed for other biomass precursors, such as aloe vera, sugarcane bagasse, human hair, and poplar catkin [15,16,18,28], which demonstrated that the utilization of an optimized activation temperature was the key to obtain biochar with optimum pore structure for supercapacitor applications. Besides activating the biochar by using KOH, other activation reagents, such as ZnCl_2 and CaCl_2 , were also used for the activation process [13,36]. However, it was not a surprise to discover that by keeping the other activation parameters constant, the pore structures of the activated carbon obtained from ZnCl_2 and KOH showed substantial differences in SSA and the ratio between micropores and mesopores ($R_{\text{micro/meso}}$) [36]. Significantly higher SSA ($\sim 1578 \text{ m}^2 \text{ g}^{-1}$) and $R_{\text{micro/meso}} = 2.56$ were obtained for the biochar activated by KOH (SSA = $985 \text{ m}^2 \text{ g}^{-1}$ and $R_{\text{micro/meso}} = 1.09$ for the case of ZnCl_2), which showed obviously better supercapacitor performance. On the other hand, the KOH activation can also combine with physical activation (e.g., CO_2 activation) and the co-addition of heteroatom source such as melamine and thiourea, which can simultaneously generate the biochar with controlled surface functional groups and heteroatom doping that remarkably enhance the material supercapacitive performance [13,29,31,33]. Furthermore, novel synthesis methods such as chemical blowing can be combined with the KOH activation to give ultramicroporous carbon nitride frameworks with excellent supercapacitive properties [118]. While engineering over the meso/microporous structures of the carbon materials can also be achieved through the usage of mesoporous hard template (FDU-12) and the precursors with preorganized molecular structures, respectively [119,120].

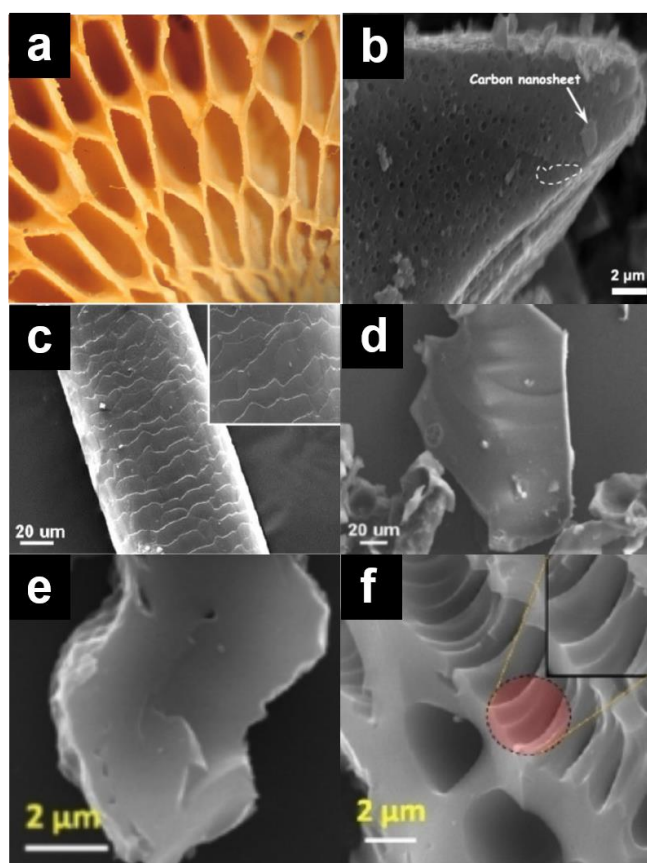


Figure 8. SEM images showing the microstructures of the precursors and the corresponding biomass-derived carbons, including (a) the hymenium of auricularia. Reproduced from [121], with permission from Elsevier, 2007; and (b) the porous layer-stacking carbon. Reproduced from [26], with permission from Elsevier, 2015; (c) human hair and (d) the micro/mesoporous carbon. Reproduced from [18], with permission from Royal Society of Chemistry, 2014; the carbonized orange peel before (e) and after (f) KOH activation. Reproduced from [122], with permission from John Wiley and Sons, 2017. The magnified SEM images in c and f showed the enlarged view of the hair-surface feature and the porous structure of the activated orange peel, respectively.

For supercapacitor applications, the activated carbon with high SSA and PV, and interconnected meso/microporous structures are undoubtedly preferred. Since the carbon materials store charges mainly through the electrical double-layer mechanism, high SSA and PV can significantly increase the electrode–electrolyte interfaces to promote the electrical double-layer formation, and remarkably enhance the specific capacitance and rate performance of the carbon materials. This is especially the case for the activated carbon with interconnected meso/microporous structure, as the diffusion of electrolyte into the micropores can be effectively promoted through the interconnected mesopore pathways. Thus, the activation process may have significant impact on the performance of the biomass-derived carbons used in supercapacitors. To prepare biomass-derived carbon with superior supercapacitive performance, the following criteria should be considered: (i) the precursors with intrinsic porous structures, especially interconnected meso/microporous structures are preferred; (ii) the intrinsic microporous structures are preserved as the precursors are converted to carbon during the carbonization and activation process; (iii) low KOH/C mass ratio ($\sim 1\text{--}3$) and longer activation time are suggested for the activation process in the appropriate temperature range ($700\text{--}900\text{ }^{\circ}\text{C}$). To further compare the performance of different biomass-derived carbons in supercapacitor applications and their structure–property relationship, a detailed comparative study is presented in Table 8 [122–128].

According to Table 8, it can be clearly observed that the biomass-derived carbons that are activated show higher specific capacitance, higher SSA and PV, and better rate performance. This

phenomenon can be attributed to the well-developed microporosity within the porous carbon framework created from the KOH etching. Compared with KOH, ZnCl_2 is not as efficient in permeating the carbon lattice and generating micropores due to the relatively large radius of Zn^{2+} ions. And the metallic Zn produced from the reaction between Zn^{2+} and C is tended to induced the formation of amorphous carbon structures [129], which lower the material conductivity and deteriorate the material performance in supercapacitors. On the other hand, among the KOH activated biomass-derived carbons, the carbon structures obtained from low KOH/C mass ratio (between 1:1 and 3:1) show higher specific capacitance, cycling stability and rate performance (i.e., auricularia, human hair, orange peel), indicating high accessibility of the electrolyte to the microporous structures, and the rapid formation of the electrical double layer inside the pores, which can be attributed to the generation of interconnected meso/microporous structure within the carbon framework by the mild KOH etching. It is also worthy of noticing that there exists an optimum activation temperature for producing biomass-derived carbons at constant KOH/C ratios and activation time. The structural parameters, such as SSA and PV, cannot be optimized if the activation temperature is either too high or too low. However, the operational temperature range for the KOH activation process is reported to be between 700 and 900 °C. It is also worthy of mention that the structures of the biomass-derived carbons are closely related to the microstructures of the precursor. For example, the porous layer stacking carbon derived from auricularia shows similar structural characteristics to the hymenium of auricularia, which resembles a hierarchical structure composed of relatively ordered stacking layers, as shown in Figure 8a,b. And the micro/mesoporous carbon derived from human hair also shows similar sheet-like structures to the hair cuticles (Figure 8c,d). The orange peel derived carbon also exhibits similar 3D nanoporous structures to the orange peel, which further develop substantial interconnected meso/microporous structures upon activation (Figure 8e,f). The interconnected meso/microporous structures may also provide better supercapacitor performance in terms of higher power density and energy density theoretically [130]. By assuming the mesopores of the biomass-derived carbon are cylindrical, the capacitance of the electrical double-cylinder capacitors (EDCC) formed inside the mesopores can be given by [131]:

$$C/A = \frac{\epsilon_r \epsilon_0}{b \ln(\frac{b}{b-d})} \quad (1)$$

where C is the capacitance, A is the surface area of the cylinder, ϵ_r is the dielectric constants of the electrolyte and ϵ_0 is the permittivity of the vacuum. b is the radius of the outer cylinder, a is the radius of the inner cylinder, and d is the separation distance of the outer and inner cylinders, as shown in Figure 9a.

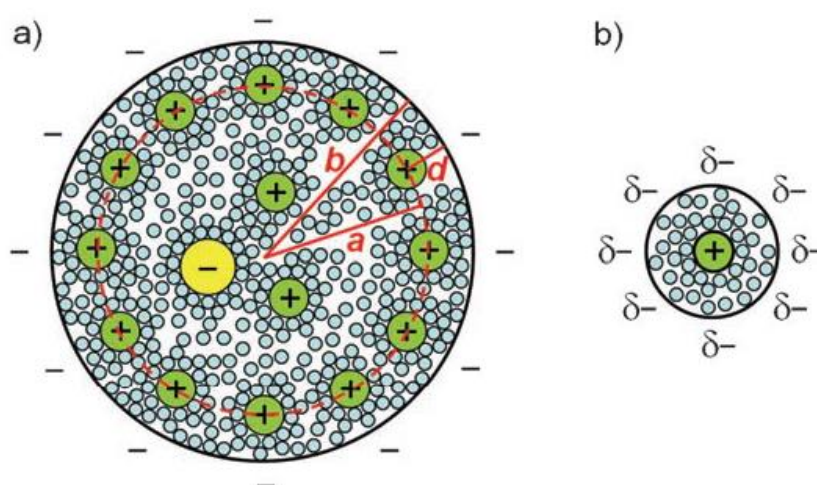


Figure 9. Schematic illustration of a negatively charged mesopore (a) and micropore (b). The solvated cations migrate towards the wall of the cylindrical mesopore to form the electric

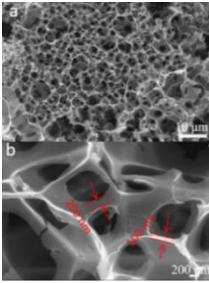
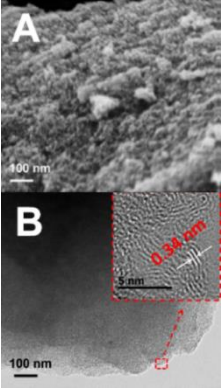
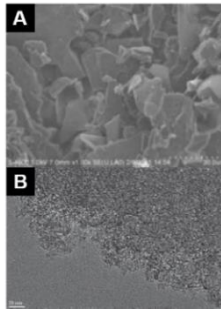
double-cylinder capacitor with an outer radius of b and an inner radius of a . In the case of micropore, the solvated cation with a radius of a_0 occupies the pore volume and form the electric wire-in-cylinder capacitor. Reproduced from [132], with permission from John Wiley and Sons, 2008.

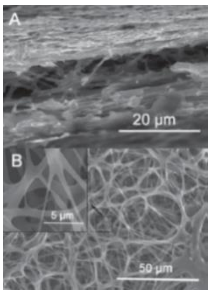
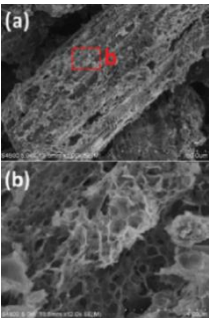
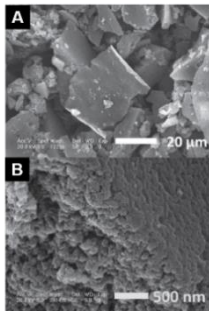
In this case, to achieve a larger value of C , the distance of the double cylinder d should be as small as possible, which means the size of the mesopore should be carefully engineered to fit the diffusion coefficients of the counterions. In the case of micropores, the counterions will form an electric wire-in-cylinder capacitor (EWCC) instead of EDCC due to the extremely small pore size, as shown in Figure 9b. And the capacitance of the EWCC can be given by [132]:

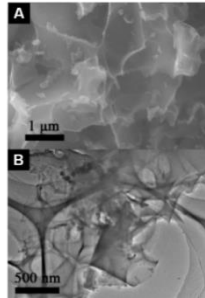
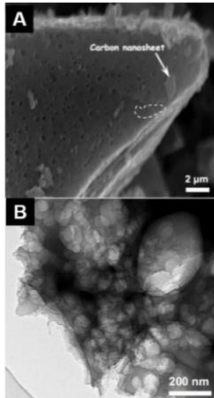
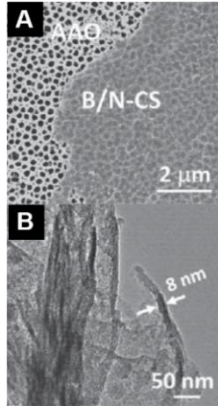
$$C/A = \frac{\epsilon_r \epsilon_0}{b_0 \ln(\frac{b_0}{a_0})} \quad (2)$$

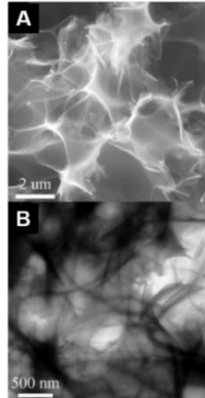
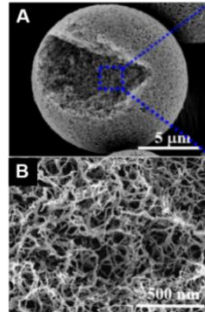
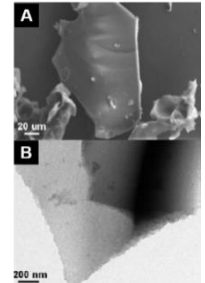
where b_0 is the radius of the cylinder and a_0 is the effective size of the counterions. Therefore, the ratio between b_0 and a_0 should be carefully adjusted to enhance the EWCC capacitance of the micropore. In other words, the radius of the micropore should be closely adapted to the effective size of the electrolyte ions to obtain optimized capacitance performance [133].

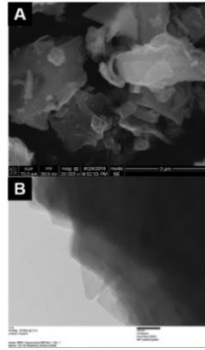
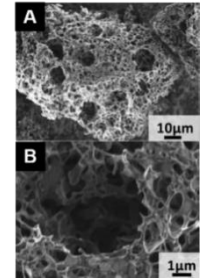
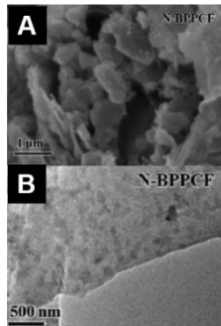
Table 8. The supercapacitor performance and the related structural parameters of biomass-derived carbon produced from different plant-, fruit-, microorganism- and animal-based precursors (the rate performance of the materials are referred to the percentage remain of the specific capacitance shown in the sixth column at the elevated current density).

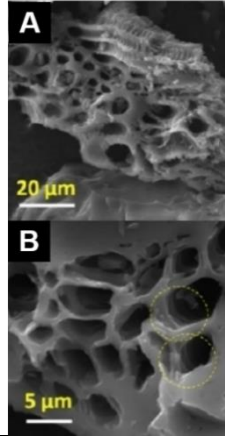
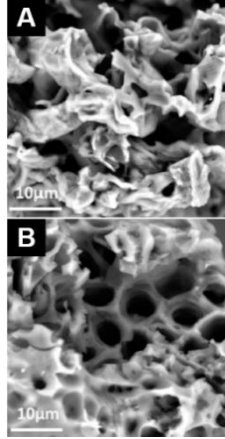
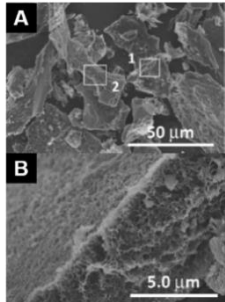
Precursor	Biomass-Derived Carbon Produced	Activation Method	Specific Surface Area ($\text{m}^2 \text{g}^{-1}$)	Pore Volume ($\text{cm}^3 \text{g}^{-1}$)	Specific Capacitance	Current Density	Cycling Stability	Microstructure	Rate Performance & Conductivity
Wheat flour [123]	Hierarchically porous nitrogen-doped carbon (HPC)	KOH/C = 1:1, 800 °C, 2 h	1294	N/A	383 F g^{-1}	1 A g^{-1}	91.6% after 5000 cycles		~65% at 10 A g^{-1} Figure caption: (a,b) SEM images of HPC.
Poplar catkin [28]	Nitrogen and oxygen dual doped carbon (NODC)	ZnCl ₂ /C = 3:1, 800 °C, 2 h	1462.5	1.31	251 F g^{-1}	0.5 A g^{-1}	~100% after 1000 cycles		~68% at 30 A g^{-1} (A) SEM and (B) TEM images of NODC-800.
Chicken egg white [30]	Egg white-derived activated carbon (eAC)	KOH/C = 3:1, 900 °C, 3 h	3250	1.97	56 F g^{-1}	12.8 A g^{-1}	79.2% after 15,000 cycles		N/A (A) SEM and (B) TEM images of eAC-900. Scale bar: (A) 30 μm, (B) 20 nm.

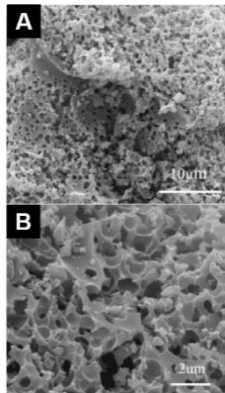
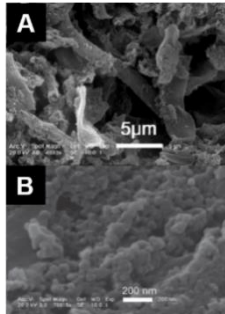
Chicken eggshell membrane [24]	Carbonized eggshell membrane (CESM)	Activated in air at 300 °C, 2 h	221.2	0.13	297 F g ⁻¹	0.2 A g ⁻¹	97% after 10,000 cycles		66% at 20 A g ⁻¹ , 8.9 × 10 ⁻⁴ Ω m (A,B) SEM images of activated CESM.
Bamboo char [124]	Porous graphitic biomass carbon (PGBC)	K ₂ FeO ₄ /C≈2:1, 800 °C, 2 h	1732	0.97	222.0 F g ⁻¹	0.5 A g ⁻¹	84% after 5000 cycles (solid-state)		51.8% at 20 A g ⁻¹ , 4.7 S cm ⁻¹ (a,b) SEM images of PGBC-1. Scale bar: (a) 50 µm, (b) 4 µm.
<i>Bacillus subtilis</i> [36]	Heteroatom-doped carbon (HDC)	KOH/C = 4:1, 800 °C, 2 h	1578	1.092	310 F g ⁻¹	0.2 A g ⁻¹	96% after 1200 cycles		64.5% at 10 A g ⁻¹ (A,B) SEM images of HDC activated by ZnCl ₂ .

Willow catkin [29]	<i>N,S</i> -co-doped porous carbon nanosheet (<i>N,S</i> -PCN)	KOH/willow catkin = 1:1, 400 °C for 3 h, and then 850 °C for 1 h, and then 300 °C in air for 1 h	1533	0.92	298 F g ⁻¹	0.5 A g ⁻¹	98% after 10,000 cycles		78.2% at 50 A g ⁻¹ (A) SEM and (B) TEM images of <i>N,S</i> -PCN.
<i>Auricularia</i> [26]	Porous graphene-like carbon (PGC)	One-pot hydrothermal carbonization and activation, KOH/fungus ≈ 0.14:1	1103	0.54	374 F g ⁻¹	0.5 A g ⁻¹	99% after 10,000 cycles		78% at 5 A g ⁻¹ (A) SEM and (B) TEM images of PGC.
Gelatin [25]	B/N co-doped carbon nanosheets (B/N-CS)	Not activated	416	0.76	358 F g ⁻¹	0.1 A g ⁻¹	113% after 15,000 cycles		74.6% at 30 A g ⁻¹ , 9.8 S m ⁻¹ (A) SEM image of B/N-CS on AAO and (B) Cross-section TEM image of B/N-CS.

Dry elm samara [19]	Porous carbon nanosheets (PCNS)	One-pot carbonization and activation, KOH/dry elm samara \approx 3.4:1, 700 °C, 2 h	1947	1.33	470 F g ⁻¹	1 A g ⁻¹	98% after 50,000 cycles		63.8% at 10 A g ⁻¹ (A) SEM and (B) TEM images of PCNS-6.
Chitin [27]	Nitrogen-doped nanofibrous carbon microspheres (NCM)	Not activated	1141	-	219 F g ⁻¹	5 mV s ⁻¹	96% after 10,000 cycles		50% at 10,000 mV s ⁻¹ (A,B) SEM images of NCM-900
Human hair [18]	Heteroatom-doped porous carbon flakes (HMC)	KOH/C = 2:1, 800 °C, 2 h	1306	0.90	445 F g ⁻¹	0.5 A g ⁻¹	98% after 20,000 cycles		51% at 10 A g ⁻¹ , 47.3 S m ⁻¹ (A) SEM and (B) TEM images of HMC-800

Oil tea shell [125]	Activated carbon (AC)	One-pot carbonization and activation, ZnCl ₂ /oil tea shell = 3:1	2851	2.68	146 F g ⁻¹	0.5 A g ⁻¹	86% after 3000 cycles		86.6% at 4 A g ⁻¹ (A) SEM and TEM images of AC. Scale bar: (A) 3 μm, (B) 100 nm.
Fig-fruit: inner part [126]	Highly porous foam-like carbon	One-pot carbonization and activation, KOH/fig-fruit = 3:1, 900 °C, 2 h	2337	1.005	340 F g ⁻¹	0.5 A g ⁻¹	>100% after 10,000 cycles		50% at 50 A g ⁻¹ (A,B) SEM images of the fig-fruit inner part after activation
Banana peel [127]	Nitrogen-doped porous carbon foam (N-BPPCF)	Not activated	1357.6	0.77	210.6 F g ⁻¹	0.5 A g ⁻¹	~100% after 5000 cycles		79.7% at 50 mV s ⁻¹ (A) SEM and (B) TEM images of N-BPPCF.

Orange peel [122]	3D nanoporous carbon	KOH/C = 3:1, 600 °C, 1 h	2160	0.779	460 F g ⁻¹	1 A g ⁻¹	98% after 10,000 cycles		59% at 100 A g ⁻¹ (A,B) SEM images of the orange-peel derived activated carbon.
Orange peel [20]	Interconnected hollow-structure d carbon (OPAC)	KOH/C = 1:1, 800 °C, 2 h	1391	0.72	407 F g ⁻¹	0.5 A g ⁻¹	100% after 5000 cycles		~37% at 20 A g ⁻¹ SEM images of OPAC-1 (A) and OPAC-2 (B). Nos. 1 and 2 represent the KOH/C ratios.
Shiitake mushroom [42]	Hierarchically porous activated carbon (KPAC)	KOH/C = 3:1, 800 °C, 2 h	2988	1.76	306 F g ⁻¹	1 A g ⁻¹	95.7% after 15,000 cycles		78.4% at 30 A g ⁻¹ (A,B) SEM images of KPAC-800.

Kombucha [35]	Hierarchical porous carbon (KHPC)	KOH:C = 0.6:1, 700 °C, 1 h	917	0.41	326 F g ⁻¹	1 A g ⁻¹	91.3% after 5000 cycles		82% at 20 A g ⁻¹ (A,B) SEM images of KHPC.
Crude auricularia [128]	Pyrolyzed hydrothermally carbonized auricularia (P-HT-A)	Not activated	80.08	0.496	196 F g ⁻¹	5 mV s ⁻¹	91.8% after 1000 cycles		~31% at 200 mV s ⁻¹ SEM images of (A) HT-A and (B) P-HT-A.

4. Conclusions and Perspectives

In conclusion, the utilization of naturally abundant biomass to prepare biomass-derived carbons with high functional performance in supercapacitor application is green, cost-saving and sustainable. However, the processability, final structure, and functional performance of the as-prepared biomass-derived carbon is strongly correlated with the chemical composition, macroscopic structural hierarchy, and the sublevel microstructural characteristics of the biomass precursors. Thus, it requires rational design in the processes of precursor selection, carbonization, and activation to obtain high-performance biomass-derived carbon with optimized SSA, PV, specific capacitance and conductivity for supercapacitor applications. Even though the state-of-the-art research on the biomass-derived carbon for supercapacitors has shown relatively higher specific capacitances compared to conventional carbon nanomaterials (e.g., CNT, CNF), and excellent high-rate performance and cyclability, several critical challenges are still associated with the development of biomass-derived carbon for supercapacitors:

(i) The carbon yield: it has been mentioned in the context that the carbon yields of the biomass differed according to the chemical and elemental compositions of the precursor, which were in the range between 5.5 and 52.1 wt%. It thus raises a serious concern that some of the biomass-derived carbons with excellent supercapacitive properties are obtained from low-carbon-yield precursors, which in turn substantially limit their large-scale production.

To address this issue, pretreatments can be applied to the biomass precursors to improve their carbonization efficiency. For example, the major carbon contributors such as lignin, chitin and keratin can be extracted from the precursors, then purified and concentrated prior to the carbonization to achieve a high carbon yield [27,31,40]. On the other hand, improvements over the carbonization and activation processes can also be implemented, including combined the carbonization and activation in one pot by the proper mixing of KOH and the precursor [19,26,126]; metallic catalysts, and organic compounds can also mix with the biomass precursor to direct the graphitic structure formation and provide additional carbon source during carbonization, respectively [31,32,41].

(ii) The energy density: even though the specific capacitance of the biomass-derived carbons can reach relatively high values above 400 F g^{-1} , they are still not comparable with the pseudocapacitive materials which can reach specific capacitance above 1000 F g^{-1} [134]. In other words, the biomass-derived carbons may attain the intrinsic drawbacks of electric double-layer capacitors such as lowered specific capacitance and energy density. To address this issue, heteroatom doping—such as N, S, B, O—can be introduced to the biomass-derived carbons by adding the heteroatom containing organic compounds either before or after the carbonization process [25,29,123]. On the other hand, nanocomposites of biomass-derived carbons with significantly enhanced energy density can also be obtained from the post-synthesis processes such as coating with conducting polymers and metal oxides [41,123,135].

(iii) Carbon microstructural control: until now, the synthesis and formation of biomass-derived carbons almost always followed the unattended process, which means there lacks engineering control over the carbonization and graphitization processes of the biomass precursors. The consequence of this ignorance causes a random arrangement of the graphitized structures over the biomass-derived carbons, and a random distribution of the macro-, meso- and micropores over the carbonized biomass, which in turn substantially lowers the charge transport efficiency and ion transport efficiency. To address this issue, engineering techniques should be applied over the carbonization process of the biomass precursors to control the orientation of the graphitized carbon and the pore distribution. For example, blowing reagents (e.g., NH_4Cl) can be added during the carbonization process to obtain ultramicroporous carbon with graphene walls [118]; nanostructured templates, such as phenolic resins, silica, and metal-organic frameworks, can be integrated with the biomass precursors during carbonization to obtain microporous carbon with ordered pore size distribution [119,130,136]. On the other hand, the KOH activation can also be replaced by other highly efficient activation techniques such as air activation and hydrothermal activation, to obtain biomass-derived carbons with improved nitrogen contents and self-supporting properties [24,25].

Author Contributions: Y.L. was responsible for the literature search, data analysis and manuscript preparation. J.C., B.C. and P.Y. were responsible for the data mining from the literatures. C.Z. was responsible for the biochemical structure analysis and modelling.

Funding: This research was funded by China Postdoctoral Science Foundation, grant number [2018M633230].

Acknowledgments: The authors gratefully acknowledge the financial support from Sun Yat-sen University.

Conflicts of Interest: The authors declare no conflicts of interest.

References

1. Nover, G.; Stoll, J.B.; Gonna, J. Promotion of graphite formation by tectonic stress—A laboratory experiment. *Geophys. J. Int.* **2005**, *160*, 1059–1067.
2. Stachel, T.; Harris, J.W. Formation of diamond in the Earth's mantle. *J. Phys. Condens. Matter* **2009**, *21*, 364206.
3. De, S.; Balu, A.M.; Waal, J.C.; Luque, R. Biomass-Derived Porous Carbon Materials: Synthesis and Catalytic Applications. *ChemCatChem* **2015**, *7*, 1608–1629.
4. Jung, S.; Myung, Y.; Kim, B.N.; Kim, I.G.; You, I.K.; Kim, T.Y. Activated Biomass-derived Graphene-based Carbons for Supercapacitors with High Energy and Power Density. *Sci. Rep.* **2018**, *8*, 1915.
5. Simon, P.; Gogotsi, Y. Charge storage mechanism in nanoporous carbons and its consequence for electrical double layer capacitors. *Philos. Trans. R. Soc. A Math. Phys. Eng. Sci.* **2010**, *368*, 3457–3467.
6. Mahmoud, A.; Olivier, J.; Vaxelaire, J.; Hoadley, A.F.A. Electrical field: A historical review of its application and contributions in wastewater sludge dewatering. *Water Res.* **2010**, *44*, 2381–2407.
7. Madhu, R.; Veeramani, V.; Chen, S. Heteroatom-enriched and renewable banana-stem-derived porous carbon for the electrochemical determination of nitrite in various water samples. *Sci. Rep.* **2014**, *4*, 4679.
8. Chen, S.; Tang, S.; Sun, Y.; Wang, G.; Chen, H.; Yu, X.; Su, Y.; Chen, G. Preparation of a Highly Porous Carbon Material Based on Quinoa Husk and Its Application for Removal of Dyes by Adsorption. *Materials* **2018**, *11*, 1407.
9. Wang, Y.; Shen, F.; Qi, X. A corn stalk-derived porous carbonaceous adsorbent for adsorption of ionic liquids from aqueous solution. *RSC Adv.* **2016**, *6*, 32505.
10. Wang, R.; Wang, P.; Yan, X.; Lang, J.; Peng, C.; Xue, Q. Promising Porous Carbon Derived from Celtuce Leaves with Outstanding Supercapacitance and CO₂ Capture Performance. *ACS Appl. Mater. Interfaces* **2012**, *4*, 5800–5806.
11. Jalilov, A.S.; Ruan, G.; Hwang, C.C.; Schipper, D.E.; Tour, J.J.; Li, Y.; Fei, H.; Samuel, E.L.G.; Tour, J.M. Asphalt-Derived High Surface Area Activated Porous Carbons for Carbon Dioxide Capture. *ACS Appl. Mater. Interfaces* **2015**, *7*, 1376–1382.
12. Liang, T.; Chen, C.; Li, X.; Zhang, J. Popcorn-Derived Porous Carbon for Energy Storage and CO₂ Capture. *Langmuir* **2016**, *32*, 8042–8049.
13. Chen, F.; Ma, L.; Ren, J.; Zhang, M.; Luo, X.; Li, B.; Song, Z.; Zhou, X. Wheat Straw-Derived N-, O-, and S-Tri-doped Porous Carbon with Ultrahigh Specific Surface Area for Lithium-Sulfur Batteries. *Materials* **2018**, *11*, 989.
14. Xu, X.; Zhou, J.; Nagaraju, D.H.; Jiang, L.; Marinov, V.R.; Lubineau, G.; Alshareef, H.N.; Oh, M. Flexible, Highly Graphitized Carbon Aerogels Based on Bacterial Cellulose/Lignin: Catalyst-Free Synthesis and its Application in Energy Storage Devices. *Adv. Funct. Mater.* **2015**, *25*, 3193–3202.
15. Wahid, M.; Puthusseri, D.; Phase, D.; Ogale, S. Enhanced Capacitance Retention in a Supercapacitor Made of Carbon from Sugarcane Bagasse by Hydrothermal Pretreatment. *Energy Fuels* **2014**, *28*, 4233–4240.
16. Karnan, M.; Subramani, K.; Sudhan, N.; Ilayaraja, N.; Sathish, M. Aloe vera Derived Activated High-Surface-Area Carbon for Flexible and High-Energy Supercapacitors. *ACS Appl. Mater. Interfaces* **2016**, *8*, 35191–35202.
17. Rana, M.; Subramani, K.; Sathish, M.; Gautam, U.K. Soya Derived Heteroatom Doped Carbon as a Promising Platform for Oxygen Reduction, Supercapacitor and CO₂ Capture. *Carbon* **2017**, *114*, 679–689.
18. Qian, W.; Sun, F.; Xu, Y.; Qiu, L.; Liu, C.; Wang, S.; Yan, F. Human hair-derived carbon flakes for electrochemical supercapacitors. *Energy Environ. Sci.* **2014**, *7*, 379.

19. Chen, C.; Yu, D.; Zhao, G.; Du, B.; Tang, W.; Sun, L.; Sun, Y.; Besenbacher, F.; Yu, M. Three-dimensional scaffolding framework of porous carbon nanosheets derived from plant wastes for high-performance supercapacitors. *Nano Energy* **2016**, *27*, 377–389.
20. Ranaweera, C.K.; Kahol, P.K.; Ghimire, M.; Mishra, S.R.; Gupta, R.K. Orange-Peel-Derived Carbon: Designing Sustainable and High-Performance Supercapacitor Electrodes. *J. Carbon Res.* **2017**, *3*, 25.
21. Dang, Y.Q.; Ren, S.Z.; Liu, G.; Cai, J.; Zhang, Y.; Qiu, J. Electrochemical and Capacitive Properties of Carbon Dots/Reduced Graphene Oxide Supercapacitors. *Nanomaterials* **2016**, *6*, 212.
22. McDonough, J.R.; Choi, J.W.; Yang, Y.; Mantia, F.L.; Zhang, Y.; Cui, Y. Carbon Nanofiber Supercapacitors with Large Areal Capacitances. *Appl. Phys. Lett.* **2009**, *95*, 243109.
23. Yoon, J.; Lee, J.; Hur, J. Stretchable Supercapacitors Based on Carbon Nanotubes-Deposited Rubber Polymer Nanofibers Electrodes with High Tolerance against Strain. *Nanomaterials* **2018**, *8*, 541.
24. Li, Z.; Zhang, L.; Amirkhiz, B.S.; Tan, X.; Xu, Z.; Wang, H.; Olsen, B.C.; Holt, C.M.B.; Mitlin, D. Carbonized Chicken Eggshell Membranes with 3D Architectures as High-Performance Electrode Materials for Supercapacitors. *Adv. Energy Mater.* **2012**, *2*, 431–437.
25. Ling, Z.; Wang, Z.; Zhang, M.; Yu, C.; Wang, G.; Dong, Y.; Liu, S.; Wang, Y.; Qiu, J. Sustainable Synthesis and Assembly of Biomass-Derived B/N Co-Doped Carbon Nanosheets with Ultrahigh Aspect Ratio for High-Performance Supercapacitors. *Adv. Funct. Mater.* **2016**, *26*, 111–119.
26. Long, C.; Chen, X.; Jiang, L.; Zhi, L.; Fan, Z. Porous layer-stacking carbon derived from in-built template in biomass for high volumetric performance supercapacitors. *Nano Energy* **2015**, *12*, 141–151.
27. Duan, B.; Gao, X.; Yao, X.; Fang, Y.; Huang, L.; Zhou, J.; Zhang, L. Unique elastic N-doped carbon nanofibrous microspheres with hierarchical porosity derived from renewable chitin for high rate supercapacitors. *Nano Energy* **2016**, *27*, 482–491.
28. Gao, S.; Li, X.; Li, L.; Wei, X. A versatile biomass derived carbon material for oxygen reduction reaction, supercapacitors and oil/water separation. *Nano Energy* **2017**, *33*, 334–342.
29. Li, Y.; Wang, G.; Wei, T.; Fan, Z.; Yan, P. Nitrogen and sulfur co-doped porous carbon nanosheets derived from willow catkin for supercapacitors. *Nano Energy* **2016**, *19*, 165–175.
30. Li, B.; Dai, F.; Xiao, Q.; Yang, L.; Shen, J.; Zhang, C.; Cai, M. Activated Carbon from Biomass Transfer for High-Energy Density Lithium-Ion Supercapacitors. *Adv. Energy Mater.* **2016**, *6*, 1600802.
31. Zhu, L.; Shen, F.; Smith, R.L.; Yan, L.; Li, L.; Qi, X. Black liquor-derived porous carbons from rice straw for high-performance supercapacitors. *Chem. Eng. J.* **2017**, *316*, 770–777.
32. Liu, W.; Mei, J.; Liu, G.; Kou, Q.; Yi, T.; Xiao, S. Nitrogen-Doped Hierarchical Porous Carbon from Wheat Straw for Supercapacitors. *ACS Sustain. Chem. Eng.* **2018**, *6*, 11595–11605.
33. Hu, C.C.; Wang, C.C.; Wu, F.C.; Tseng, R.L. Characterization of Pistachio Shell-derived Carbons Activated by a Combination of KOH and CO₂ for Electric Double-layer Capacitors. *Electrochim. Acta* **2007**, *52*, 2498–2505.
34. Su, X.; Cheng, M.; Fu, L.; Yang, J.; Zheng, X.; Guan, X. Superior Supercapacitive Performance of Hollow Activated Carbon Nanomesh with Hierarchical Structure Derived from Poplar Catkins. *J. Power Sources* **2017**, *362*, 27–38.
35. Dai, C.; Wan, J.; Geng, W.; Song, S.; Ma, F.; Shao, J. KOH direct treatment of kombucha and in situ activation to prepare hierarchical porous carbon for high-performance supercapacitor electrodes. *J. Solid State Electrochem.* **2017**, *21*, 2929–2938.
36. Zhu, H.; Yin, J.; Wang, X.; Wang, H.; Yang, X. Microorganism-Derived Heteroatom-Doped Carbon Materials for Oxygen Reduction and Supercapacitors. *Adv. Funct. Mater.* **2013**, *23*, 1305–1312.
37. Li, F.; Qin, F.; Zhang, K.; Fang, J.; Lai, Y.; Li, J. Hierarchically porous carbon derived from banana peel for lithium sulfur battery with high areal and gravimetric sulfur loading. *J. Power Sources* **2017**, *362*, 160–167.
38. Sudhan, N.; Subramani, K.; Karnan, M.; Ilayaraja, N.; Sathish, M. Biomass-Derived Activated Porous Carbon from Rice Straw for a High-Energy Symmetric Supercapacitor in Aqueous and Nonaqueous Electrolytes. *Energy Fuels* **2017**, *31*, 977–985.
39. Karnan, M.; Subramani, K.; Srividhya, P.K.; Sathish, M. Electrochemical Studies on Corncob Derived Activated Porous Carbon for Supercapacitors Application in Aqueous and Non-aqueous Electrolytes. *Electrochim. Acta* **2017**, *228*, 586–596.
40. Berenguer, R.; Garcia-Mateos, F.J.; Ruiz-Rosas, R.; Cazorla-Amoros, D.; Morallon, E.; Rodriguez-Mirasol, J.; Cordero, T. Biomass-derived Binderless Fibrous Carbon Electrodes for Ultrafast Energy Storage. *Green Chem.* **2016**, *18*, 1506.

41. Zhong, Y.; Xia, X.; Deng, S.; Zhan, J.; Fang, R.; Xia, Y.; Wang, X.; Zhang, Q.; Tu, J. Popcorn Inspired Porous Macrocellular Carbon: Rapid Puffing Fabrication from Rice and Its Applications in Lithium-Sulfur Batteries. *Adv. Energy Mater.* **2018**, *8*, 1701110.
42. Cheng, P.; Gao, S.; Zang, P.; Yang, X.; Bai, Y.; Xu, H.; Liu, Z.; Lei, Z. Hierarchically porous carbon by activation of shiitake mushroom for capacitive energy storage. *Carbon* **2015**, *93*, 315–324.
43. Hao, R.; Yang, Y.; Wang, H.; Jia, B.; Ma, G.; Yu, D.; Guo, L. Direct chitin conversion to N-doped amorphous carbon nanofibers for high-performing full sodium-ion batteries. *Nano Energy* **2018**, *45*, 220–228.
44. Rath, N.C.; Makkar, S.; Packialakshmi, B.; Donoghue, A.M. Egg Shell Membrane Improves Immunity of Post Hatch Poultry: A Paradigm for Nutritional Immunomodulation. United States Department of Agriculture. Available online: <https://www.ars.usda.gov/alternativestoantibiotics/Symposium2016/includes/Oral%20Presentations/4%20-%20Immune%20Related%20Products/pdfs/3%20RathATA%20symposiumFinal.pdf> (accessed on 17 August 2018).
45. Yang, T.; Qian, T.; Wang, M.; Shen, X.; Xu, N.; Sun, Z.; Yan, C. A Sustainable Route from Biomass Byproduct Okara to High Content Nitrogen-Doped Carbon Sheets for Efficient Sodium Ion Batteries. *Adv. Mater.* **2016**, *28*, 539–545.
46. Zhou, X.; Chen, F.; Bai, T.; Long, B.; Liao, Q.; Ren, Y.; Yang, J. Interconnected Highly Graphitic Carbon Nanosheets Derived from Wheat Stalk as High Performance Anode Materials for Lithium Ion Batteries. *Green Chem.* **2016**, *18*, 2078.
47. Arsene, M.A.; Bilba, K.; Savastano, H.; Ghavami, K. Treatments of Non-wood Plant Fibres Used as Reinforcement in Composite Materials. *Mater. Res.* **2013**, *16*, 903–923.
48. Kumar, R.; Mago, G.; Balan, V.; Wyman, C.E. Physical and chemical characterizations of corn stover and poplar solids resulting from leading pretreatment technologies. *Bioresour. Technol.* **2009**, *100*, 3948–3962.
49. Biswas, R.; Uellendahl, H.; Ahring, B.K. Wet Explosion: A Universal and Efficient Pretreatment Process for Lignocellulosic Biorefineries. *Bioenergy Res.* **2015**, *8*, 1101–1116.
50. Daud, W.M.A.; Ali, W.S.W. Comparison on pore development of activated carbon produced from palm shell and coconut shell. *Bioresour. Technol.* **2004**, *93*, 63–69.
51. Zanzi, R.; Sjostrom, K.; Bjornbom, E. Rapid pyrolysis of agricultural residues at high temperature. *Biomass Bioenergy* **2002**, *23*, 357–366.
52. Reed, A.R.; Williams, P.T. Thermal processing of biomass natural fibre wastes by pyrolysis. *Int. J. Energy Res.* **2004**, *28*, 131–145.
53. Raisanen, T.; Athanassiadis, D. Basic Chemical Composition of the Biomass Components of Pine, Spruce and Birch. Forest Refine. 2013. Available online: http://biofuelregion.se/wp-content/uploads/2017/01/1_2_IS_2013-01-31_Basic_chemical_composition.pdf (accessed on 14 August 2018).
54. Nurmi, J. Heating values of mature trees. *Acta For. Fennica* **1997**, *256*, 28.
55. Chauvet, E. Changes in the chemical composition of alder, poplar and willow leaves during decomposition in a river. *Hydrobiologia* **1987**, *148*, 35–44.
56. Corbett, D.B.; Kohan, N.; Machado, G.; Jing, C.; Nagardeolekar, A.; Bujanovic, B.M. Chemical Composition of Apricot Pit Shells and Effect of Hot-Water Extraction. *Energies* **2015**, *8*, 9640–9654.
57. Curvetto, N.R.; Figlas, D.; Matute, R.G.; Delmastro, S. Shiitake bag cultivation on sunflower seed hulls. In *Shiitake Mushroom Growers' Handbook*; MushWorld: Brighton, UK, 2005; Chapter 4, pp. 100–104.
58. Saka, S. Chemical composition and distribution. In *Wood and Cellulosic Chemistry*; Marcel Dekker, Inc.: New York, NY, USA, 1991; Chapter 2, pp. 59–88.
59. Nascimento, M.S.; Santana, A.L.; Maranhao, C.A.; Oliveira, L.S.; Bieber, L. Phenolic Extractives and Natural Resistance of Wood. In *Biodegradation—Life of Science*; Intech: London, UK, 2013; Chapter 13, pp. 349–370.
60. Rutherford, D.W.; Wershaw, R.L.; Cox, L.G. *Changes in Composition and Porosity Occurring during the Thermal Degradation of Wood and Wood Components*; Scientific Investigations Report; U.S. Geological Survey: Reston, VA, USA, 2004.
61. McDonald-Wharry, J.; Manley-Harris, M.; Pickering, K. A comparison of the charring and carbonisation of oxygen-rich precursors with the thermal reduction of graphene oxide. *Philos. Mag.* **2015**, *95*, 4054–4077.

62. Hao, R.; Lan, H.; Kuang, C.; Wang, H.; Guo, L. Superior potassium storage in chitin-derived natural nitrogen-doped carbon nanofibers. *Carbon* **2018**, *128*, 224–230.
63. Cagnon, B.; Py, X.; Guillot, A.; Stoeckli, F.; Chambat, G. Contributions of hemicellulose, cellulose and lignin to the mass and the porous properties of chars and steam activated carbons from various lignocellulosic precursors. *Bioresour. Technol.* **2009**, *100*, 292–298.
64. Cao, X.; Ro, K.S.; Libra, J.A.; Kammann, C.I.; Lima, I.; Berge, N.; Li, L.; Li, Y.; Chen, N.; Yang, J.; et al. Effects of Biomass Types and Carbonization Conditions on the Chemical Characteristics of Hydrochars. *J. Agric. Food Chem.* **2013**, *61*, 9401–9411.
65. Zhang, J.; Choi, Y.S.; Yoo, C.G.; Kim, T.H.; Brown, R.C.; Shanks, B.H. Cellulose–Hemicellulose and Cellulose–Lignin Interactions during Fast Pyrolysis. *ACS Sustain. Chem. Eng.* **2015**, *3*, 293–301.
66. Sannigrahi, P.; Ragauskas, A.J.; Tuskan, G.A. Poplar as a feedstock for biofuels: A review of compositional characteristics. *Biofuels Bioprod. Biorefin.* **2010**, *4*, 209–226.
67. Huang, H.J.; Ramaswamy, S.; Al-Dajani, W.; Tschirner, U.; Cairncross, R.A. Effect of biomass species and plant size on cellulosic ethanol: A comparative process and economic analysis. *Biomass Bioenerg.* **2009**, *33*, 234–246.
68. USDOE–Office of Energy Efficiency and Renewable Energy. Biomass Feedstock and Composition Database. 2006. Available online: http://www1.eere.energy.gov/biomass/printable_versions/feedstock_databases.html (accessed on 4 September 2009).
69. Brown, R.C. *Biorenewable Resources: Engineering New Products from Agriculture*; Iowa State Press: Ames, IA, USA, 2003.
70. Hosseinaei, O.; Harper, D.P.; Bozell, J.J.; Rials, T.G. Improving Processing and Performance of Pure Lignin Carbon Fibers through Hardwood and Herbaceous Lignin Blends. *Int. J. Mol. Sci.* **2017**, *18*, 1410.
71. Faris, A.H.; Ibrahim, M.N.M.; Rahim, A.A.; Hussin, M.H.; Brosse, N. Preparation and characterization of lignin polyols from the residues of oil palm empty fruit bunch. *BioResources* **2015**, *10*, 7339–7352.
72. Hassan, S.N.A.M.; Ishak, M.A.M.; Ismail, K.; Ali, S.N.; Yusop, M.F. Comparison Study of Rubber Seed Shell and Kernel (*Hevea brasiliensis*) as Raw Material for Bio-Oil Production. *Energy Procedia* **2014**, *52*, 610–617.
73. Latshaw, W.L.; Miller, E.C. Elemental Composition of the Corn Plant. *J. Agric. Res.* **1924**, *27*, 845–861.
74. Morais, D.R.; Rotta, E.M.; Sargi, S.C.; Bonafe, E.G.; Suzuki, R.M.; Souza, N.E.; Matsushita, M.; Visentainer, J.V. Proximate Composition, Mineral Contents and Fatty Acid Composition of the Different Parts and Dried Peels of Tropical Fruits Cultivated in Brazil. *J. Braz. Chem. Soc.* **2017**, *28*, 308–318.
75. Romelle, F.D.; Rani, P.A.; Manohar, R.S. Chemical Composition of Some Selected Fruit Peels. *Eur. J. Food Sci. Technol.* **2016**, *4*, 12–21.
76. Kasarda, D.D.; Black, D.R. Thermal Degradation of Proteins Studied by Mass Spectrometry. *Biopolymers* **1968**, *6*, 1001–1004.
77. Nawar, W.W. Thermal Degradation of Lipids: A Review. *J. Agric. Food Chem.* **1969**, *17*, 18–21.
78. Orozco, R.S.; Hernandez, P.B.; Morales, G.R.; Nunez, F.U.; Villafuerte, J.O.; Lugo, V.L.; Ramirez, N.F.; Diaz, C.E.B.; Vazquez, P.C. Characterization of Lignocellulosic Fruit Waste as an Alternative Feedstock for Bioethanol Production. *Bioresources* **2014**, *9*, 1873–1885.
79. Bandara, A.R.; Karunarathna, S.C.; Mortimer, P.E.; Hyde, K.D.; Khan, S.; Kakumyan, P.; Xu, J. First successful domestication and determination of nutritional and antioxidant properties of the red ear mushroom *Auricularia thailandica* (Auriculariales, Basidiomycota). *Mycol. Prog.* **2017**, *16*, 1029–1039.
80. Sunner, J.; Avci, R.; Richards, L.; Groenewold, G.; Ingram, J.; Arthun, M. Preservation of yeast cell morphology for scanning electron microscopy using 3.28-μm IR laser irradiation. *J. Microbiol. Methods* **2003**, *54*, 285–287.
81. Tsujikawa, K.; Kanamori, T.; Iwata, Y.; Ohmae, Y.; Sugita, R.; Inoue, H.; Kishi, T. Morphological and chemical analysis of magic mushrooms in Japan. *Forens. Sci. Int.* **2003**, *138*, 85–90.
82. Zhang, J.; Wang, X.; Li, Q.; Shang, J. K. Real time, in situ observation of the photocatalytic inactivation of *Saccharomyces cerevisiae* cells. *Mater. Sci. Eng. C* **2015**, *49*, 75–83.
83. Abou Raya, M.A.; Shalaby, M.T.; Hafez, S.A.; Alshimaa, M.H. Chemical Composition and Nutritional Potential of Some Mushroom Varieties Cultivated in Egypt. *J. Food Dairy Sci.* **2014**, *5*, 421–434.
84. Bull, A.T. Chemical Composition of Wild-type and Mutant *Aspergillus nidulans* Cell Walls. The Nature of Polysaccharide and Melanin Constituents. *J. Gen. Microbiol.* **1970**, *63*, 75–94.

85. Wang, X.M.; Zhang, J.; Wu, L.H.; Zhao, Y.L.; Li, T.; Li, J.Q.; Wang, Y.Z. A mini-review of chemical composition and nutritional value of edible wild-grown mushroom from China. *Food Chem.* **2014**, *151*, 279–285.
86. Zhou, L.X.; Yin, J.Z. Yunnan wild edible Boletus nutrition analysis and evaluation. *Edible Fungi* **2008**, *4*, 61–62.
87. Zhang, B.Q.; Chen, J. Determination and evaluation of the *Craterellus aureus* nutrients. *Edible Fungi* **2012**, *4*, 58–60.
88. Yin, J.Z.; Zhou, L.X. Analysis of nutritional components of 4 kinds of wild edible fungi in Yunnan. *Food Res. Dev.* **2008**, *29*, 133–136.
89. Zhu, X.Q.; Wang, X.J.; Xiong, Z. Nutrient analysis of the wild *Lentinula edodes*. *For. By-Prod. Spec. China* **2007**, *2*, 9–11.
90. Zhang, B.Q.; Chen, J. Determination and analysis of nutrition components in *Sarcodon aspratus*. *Food Sci.* **2011**, *32*, 299–302.
91. Liu, G.; Wang, H.; Zhou, B.H.; Guo, X.X.; Hu, X.M. Compositional analysis and nutritional studies of *Tricholoma matsutake* collected from southwest China. *J. Med. Plants Res.* **2010**, *4*, 1222–1227.
92. Diez, A.A.; Alvarez, A. Compositional and nutritional studies on two wild edible mushrooms from northwest Spain. *Food Chem.* **2001**, *75*, 417–422.
93. Arroyo, J.; Farkas, V.; Sanz, A.B.; Cabib, E. Strengthening the fungal cell wall through chitin–glucan cross-links: Effects on morphogenesis and cell integrity. *Cell. Microbiol.* **2016**, *18*, 1239–1250.
94. Peat, S. Plant Carbohydrates. *Annu. Rev. Biochem.* **1946**, *15*, 75–92.
95. Kalac, P. Chemical composition and nutritional value of European species of wild growing mushrooms: A review. *Food Chem.* **2009**, *113*, 9–16.
96. Pineda-Insuasti, J.A.; Soto-Arroyave, C.P.; Beltran, L. Stoichiometry equation to describe the growth of the *Pleurotus ostreatus* ceba-gliie-po-010606 strain. *Biotechnol. Appl.* **2014**, *31*, 48–52.
97. Sales-Campos, C.; Araujo, L.M.; Minihoni, M.T.; Andrade, M.C.N. Physiochemical analysis and centesimal composition of *Pleurotus ostreatus* mushroom grown in residues from the Amazon. *Cienc. Tecnol. Aliment. Camp.* **2011**, *31*, 456–461.
98. Moda, E.M.; Horii, J.; Spoto, M.H.F. Edible Mushroom *Pleurotus sajor-caju* Production on Washed and Supplemented Sugarcane Bagasse. *Sci. Agric.* **2005**, *62*, 27–132.
99. Latge, J.P. The cell wall: A carbohydrate armour for the fungal cell. *Mol. Microbiol.* **2007**, *66*, 279–290.
100. Schwarz, H.; Moussian, B. Electron-microscopic and genetic dissection of arthropod cuticle Differentiation. *Mod. Res. Educ. Top. Microsc.* **2007**, *3*, 316–325.
101. Arbia, W.; Arbia, L.; Adour, L.; Amrane, A. Chitin Extraction from Crustacean Shells Using Biological Methods—A Review. *Food Technol. Biotechnol.* **2013**, *51*, 12–25.
102. Rodde, R.H.; Einbu, A.; Varum, K.M. A seasonal study of the chemical composition and chitin quality of shrimp shells obtained from northern shrimp (*Pandalus borealis*). *Carbohydr. Polym.* **2008**, *71*, 388–393.
103. Liu, S.; Sun, J.; Yu, L.; Zhang, C.; Bi, J.; Zhu, F.; Qu, M.; Jiang, C.; Yang, Q. Extraction and Characterization of Chitin from the Beetle *Holotrichia parallela* Motschulsky. *Molecules* **2012**, *17*, 4604–4611.
104. Ibitoye, E.B.; Lokman, I.H.; Hezmee, M.N.M.; Goh, Y.M.; Zuki, A.B.Z.; Jimoh, A.A. Extraction and physicochemical characterization of chitin and chitosan isolated from house cricket. *Biomed. Mater.* **2018**, *13*, 025009.
105. Sajomsang, W.; Gonil, P. Preparation and characterization of α -chitin from cicada sloughs. *Mater. Sci. Eng. C* **2010**, *30*, 357–363.
106. Ahyat, N.M.; Mohamad, F.; Ahmad, A.; Azmi, A.A. Chitin and Chitosan Extraction from *Portunus pelagicus*. *Malays. J. Anal. Sci.* **2017**, *21*, 770–777.
107. Kaya, M.; Lelesius, E.; Nagrockaite, R.; Sargin, I.; Arslan, G.; Mol, A.; Baran, T.; Can, E.; Bitim, B. Differentiations of Chitin Content and Surface Morphologies of Chitins Extracted from Male and Female Grasshopper Species. *PLoS ONE* **2015**, *10*, e0115531.
108. Percot, A.; Viton, C.; Domard, A. Optimization of Chitin Extraction from Shrimp Shells. *Biomacromole* **2003**, *4*, 12–18.
109. Kovaleva, E.; Pestov, A.; Stepanova, D.; Molochnikov, L. Characterization of chitin and its complexes extracted from natural raw sources. *AIP Conf. Proc.* **2016**, *1772*, 050007.
110. Majtan, J.; Bilikova, K.; Markovic, O.; Grof, J.; Kogan, G.; Simuth, J. Isolation and characterization of chitin from bumblebee (*Bombus terrestris*). *Int. J. Biol. Macromol.* **2007**, *40*, 237–241.

111. McKittrick, J.; Chen, P.Y.; Bodde, S.G.; Yang, W.; Novitskaya, E.E.; Meyers, M.A. The Structure, Functions, and Mechanical Properties of Keratin. *JOM* **2012**, *64*, 449–468.
112. Robbins, C.R. *Chemical and Physical Behavior of Human Hair*; Springer: Berlin, Germany, 2012; Chapter 2, pp. 105–176.
113. Shavandi, A.; Silva, T.H.; Bekhit, A.A.; Bekhit, A.E.D.A. Keratin: Dissolution, extraction and biomedical application. *Biomater. Sci.* **2017**, *5*, 1699–1735.
114. Wang, B.; Yang, W.; McKittrick, J.; Meyers, M.A. Keratin: Structure, mechanical properties, occurrence in biological organisms, and efforts at bioinspiration. *Prog. Mater. Sci.* **2016**, *76*, 229–318.
115. Lv, Y.; Zhang, F.; Dou, Y.; Zhai, Y.; Wang, J.; Liu, H.; Xia, Y.; Tu, B.; Zhao, D. A comprehensive study on KOH activation of ordered mesoporous carbons and their supercapacitor application. *J. Mater. Chem.* **2012**, *22*, 93.
116. Wang, J.; Kaskel, S. KOH activation of carbon-based materials for energy storage. *J. Mater. Chem.* **2012**, *22*, 23710.
117. Ajuria, J.; Redondo, E.; Arnaiz, M.; Mysyk, R.; Rojo, T.; Goikolea, E. Lithium and sodium ion capacitors with high energy and power densities based on carbons from recycled olive pits. *J. Power Source* **2017**, *359*, 17–26.
118. Talapaneni, S.N.; Lee, J.H.; Je, S.H.; Buyukcikir, O.; Kwon, T.; Polychronopoulou, K.; Choi, J.W.; Coskun, A. Chemical Blowing Approach for Ultramicroporous Carbon Nitride Frameworks and Their Applications in Gas and Energy Storage. *Adv. Funct. Mater.* **2017**, *27*, 1604658.
119. Cha, W.S.; Talapaneni, S.N.; Kempaiah, D.M.; Joseph, S.; Lakhi, K.S.; Al-Enizi, A.M.; Park, D.H.; Vinu, A. Excellent supercapacitance performance of 3-D mesoporous carbon with large pores from FDU-12 prepared using a microwave method. *RSC Adv.* **2018**, *8*, 17017.
120. Talapaneni, S.N.; Kim, J.; Je, S.H.; Buyukcikir, O.; Oh, J.; Coskun, A. Bottom-up synthesis of fully sp² hybridized three dimensional microporous graphitic frameworks as metal-free catalysts. *J. Mater. Chem. A* **2017**, *5*, 12080.
121. Hibbett, D.S. After the gold rush, or before the flood? Evolutionary morphology of mushroom-forming fungi (Agaricomycetes) in the early 21st century. *Mycol. Res.* **2007**, *111*, 1001–1018.
122. Subramani, K.; Sudhan, N.; Karnan, M.; Sathish, M. Orange Peel Derived Activated Carbon for Fabrication of High-Energy and High-Rate Supercapacitors. *ChemistrySelect* **2017**, *2*, 11384–11392.
123. Yu, P.; Zhang, Z.; Zheng, L.; Teng, F.; Hu, L.; Fang, X. A Novel Sustainable Flour Derived Hierarchical Nitrogen-Doped Porous Carbon/Polyaniline Electrode for Advanced Asymmetric Supercapacitors. *Adv. Energy Mater.* **2016**, *6*, 1601111.
124. Gong, Y.; Li, D.; Luo, C.; Fu, Q.; Pan, C. Highly porous graphitic biomass carbon as advanced electrode materials for supercapacitors. *Green Chem.* **2017**, *19*, 4132.
125. Zhou, M.; Gomez, J.; Li, B.; Jiang, Y.B.; Deng, S. Oil tea shell derived porous carbon with an extremely large specific surface area and modification with MnO₂ for high-performance supercapacitor electrodes. *Appl. Mater. Today* **2017**, *7*, 47–54.
126. Ba, H.; Wang, W.; Pronkin, S.; Romero, T.; Baaziz, W.; Nguyen-Dinh, L.; Chu, W.; Ersen, O.; Pham-Huu, C. Biosourced Foam-Like Activated Carbon Materials as High-Performance Supercapacitors. *Adv. Sustain. Syst.* **2018**, *2*, 1700123.
127. Liu, B.; Zhang, L.; Qi, P.; Zhu, M.; Wang, G.; Ma, Y.; Guo, X.; Chen, H.; Zhang, B.; Zhao, Z.; Dai, B.; Yu, F. Nitrogen-Doped Banana Peel-Derived Porous Carbon Foam as Binder-Free Electrode for Supercapacitors. *Nanomaterials* **2016**, *6*, 18.
128. Zhu, H.; Wang, X.; Yang, F.; Yang, X. Promising Carbons for Supercapacitors Derived from Fungi. *Adv. Mater.* **2011**, *23*, 2745–2748.
129. Liu, Y.; Zhang, X.; Poyraz, S.; Zhang, C.; Xin, J.H. One-Step Synthesis of Multifunctional Zinc-Iron-Oxide Hybrid Carbon Nanowires by Chemical Fusion for Supercapacitors and Interfacial Water Marbles. *ChemNanoMat* **2018**, *4*, 546–556.
130. Wang, D.W.; Li, F.; Liu, M.; Lu, G.Q.; Cheng, H.M. 3D Aperiodic Hierarchical Porous Graphitic Carbon Material for High-Rate Electrochemical Capacitive Energy Storage. *Angew. Chem. Int. Ed.* **2008**, *47*, 373–376.
131. Tipler, P.A. *Physics for Scientists and Engineers*; Worth Publishers: New York, NY, USA, 1976; p. 769.
132. Huang, J.; Sumpter, B.G.; Meunier, V. A Universal Model for Nanoporous Carbon Supercapacitors Applicable to Diverse Pore Regimes, Carbon Materials, and Electrolytes. *Chem. Eur. J.* **2008**, *14*, 6614–6626.

133. Frackowiak, E. Carbon Materials for Supercapacitor Application. *Phys. Chem. Chem. Phys.* **2007**, *9*, 1774–1785.
134. Augustyn, V.; Simon, P.; Dunn, B. Pseudocapacitive oxide materials for high-rate electrochemical energy storage. *Energy Environ. Sci.* **2014**, *7*, 1597–1614.
135. Fang, R.; Tian, P.; Yang, X.; Luque, R.; Li, Y. Encapsulation of ultrafine metal-oxide nanoparticles within mesopores for biomass-derived catalytic applications. *Chem. Sci.* **2018**, *9*, 1854–1859.
136. Wei, J.; Liang, Y.; Hu, Y.; Kong, B.; Simon, G.P.; Zhang, J.; Jiang, S.P.; Wang, H. A Versatile Iron–Tannin-Framework Ink Coating Strategy to Fabricate Biomass-Derived Iron Carbide/Fe-N-Carbon Catalysts for Efficient Oxygen Reduction. *Angew. Chem. Int. Ed.* **2016**, *55*, 1355–1359.



© 2018 by the authors. Submitted for possible open access publication under the terms and conditions of the Creative Commons Attribution (CC BY) license (<http://creativecommons.org/licenses/by/4.0/>).